THE JOURNAL OF PHYSICAL CHEMISTRY C

pubs.acs.org/JPCC Article

Reexamination of Surface-Enhanced Raman Scattering from Gold Nanorods as a Function of Aspect Ratio and Shape

Boris N. Khlebtsov, Vitaly A. Khanadeev, Andrey M. Burov, Eric C. Le Ru, and Nikolai G. Khlebtsov*

Cite This: J. Phys. Chem. C 2020, 124, 10647−10658 Read Online

ACCESS | Metrics & More | Article Recommendations | Supporting Information

ABSTRACT: It is now believed that the near-resonance excitation of plasmonic nanoparticles is necessary to increase the Raman signal of nearby molecules. Consequently, for surface-enhanced Raman scattering (SERS) applications, researchers seek to synthesize rationally designed nanoparticles with plasmon resonances (PRs) close to the excitation wavelength. However, existing experiments show contradicting results for the dependence of the SERS enhancement on the PR wavelength. Here, we used the etching method to prepare a set of Au nanorod (AuNR) colloids with a decreasing aspect ratio. The shape morphology of the AuNRs and their concentration and width were kept constant, while the plasmon resonance was progressively decreased from 925 to 650 nm. The AuNRs were functionalized with 1,4-nitrobenzenethiol (NBT), and SERS spectra of the colloids were measured under 785 nm laser excitation. The nanorod concentration (~7×10^{10} mL^{-1}) was quantified by the atomic absorption spectroscopy and spectrophotometry combined with TEM statistical data and T-matrix simulations. The number of adsorbed NBT molecules per one nanorod (~10^4) corresponded to the effective footprint of ~0.55 nm^2 and was close to the monolayer packing density with the topological polar surface area of NBT at 0.468 nm^2. The plasmon peak position correlated weakly with the SERS response; specifically, the ratio between the SERS intensities for on- and off-resonance excitation was below 1.5. This observation contradicts the current understanding of the electromagnetic contribution to the SERS signal. In particular, our simulations agreed with the experimental data for plasmon resonance wavelengths of 785−925 nm, but for shorter wavelengths the simulations predicted an order-of-magnitude decrease in the averaged enhancement factor. In contrast to this finding, the shape morphology strongly affected the SERS response. Specifically, when the initial cigarlike AuNRs were further overgrown to yield dumbbell morphology, their SERS intensity increased 5-fold. Finally, we show that the SERS background spectra can be attributed to both the photoluminescence from AuNR ensemble and the elastic light scattering of a very weak laser background by the same AuNR ensemble.

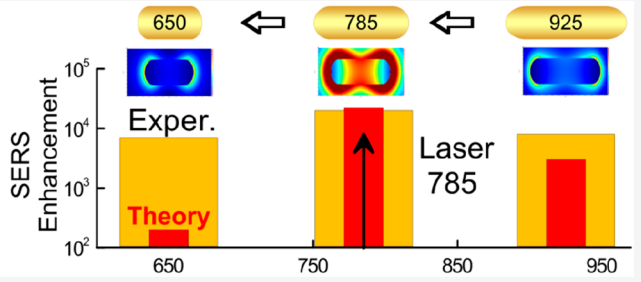

INTRODUCTION

Surface-enhanced Raman scattering (SERS) and plasmonic-based SERS tags have found promising applications in analytical and biomedical fields because of their high optical cross section, multiplexing ability, and long-term photostability.[1,2] Typically, SERS tags consist of a metal nanoparticle and Raman reporters that are adsorbed on the particle surface[3−5] or embedded inside the particle core−shell structure.[6,7] The main driving force for the SERS enhancement is the plasmonic generation of strong local electromagnetic fields ("hot spots") under appropriate light excitation.[8] It is commonly believed that the on-resonance excitation of plasmonic nanoparticles is key to the maximal enhancement of the Raman signal from nearby molecules.[9−11]

Au nanorods (AuNRs) are a convenient and flexible model to study the SERS response as a function of on- and off-resonance excitation. Owing to the particles' well-defined rodlike shape, the longitudinal plasmonic peak can easily be tuned from the visible to NIR regions by varying the nanorod aspect ratio.[12] This explains why AuNRs have been used widely as a platform to explore the relation between plasmonic and SERS properties.[13,14] In particular, several studies have been aimed at understanding the relationship between the AuNR SERS response and the plasmon resonance (PR) of AuNRs in colloids,[15−17] on substrates[18−20] and in single-particle experiments.[18,21]

Experimental results for colloids have shown somewhat inconsistent data for the enhancement factor (EF) as a function of the aspect ratio at a fixed excitation wavelength. For example, Orendorff et al.[15] and Smitha et al.[16] demonstrated that when the longitudinal surface PR of AuNRs overlaps with the laser excitation wavelength, the electromagnetic (EM)

Received: February 5, 2020
Revised: April 17, 2020
Published: April 20, 2020

https://dx.doi.org/10.1021/acs.jpcc.0c00991
J. Phys. Chem. C 2020, 124, 10647−10658

enhancement is the highest. However, Sivapalan et al.[17] obtained the highest SERS response from a suspension of AuNRs with a PR blue-shifted with respect to the laser wavelength. This observation was explained by a competition between SERS enhancement and extinction of light propagating through the sample. In contrast to colloids, the excitation SERS profiles for electron-beam lithography arrays demonstrate more consistent data. In particular, Félidj et al.[22] showed that the SERS excitation profiles for both longitudinal and transversal polarizations with respect to elongated particles follow remarkably the extinction spectra. They also noted that a phenomenological treatment predicts maximal SERS response at $\lambda_{LSPR} = (\lambda_{ex} + \lambda_{Raman})/2$. The van Duyne group[10] also observed maximal SERS enhancement at excitation wavelengths slightly shorter than the PR wavelength.

Although the crucial role of hot-spot generation and the EM contribution to the overall SERS enhancement has been established for a long time,[23] there still remains some gaps in our current understanding of the interplay between the near-field (SERS) and the far-field optical response. Indeed, the SERS EF scales like the fourth power of the local field.[24] As a result, even a small detuning of the longitudinal PR from the excitation wavelength could lead to a substantial decrease in the theoretical EF. However, the existing experimental data for AuNR colloids do not confirm such theoretical predictions. Evidently, the random orientation of AuNRs in suspensions is a complicating factor. However, the recently published single-particle data for the simple long-axis excitation of AuNRs[21] do not show any substantial variations in the EF as a function of the aspect ratio, in contradiction with current EM models.

Most previous studies have used samples of AuNRs with different diameters, particle concentrations, amounts of impurities, and probably some variations in the nanorod shape. Given the above-discussed discrepancies between calculated and measured on- and off-resonance SERS responses, we carried out a reexamination study with well-characterized AuNRs. To this end, we used controllable nanorod etching[25,26] to prepare AuNR colloids with identical concentrations, identical nanorod widths and shapes, and PR wavelengths tunable (650−925 nm) through the variation of the nanorod length and, therefore, the aspect ratio. The Raman reporter 1,4-nitrobenzenethiol (NBT) was chemisorbed on the nanorod surface, and the SERS spectra were acquired in the backscattering mode at a 785 nm excitation wavelength. For accurate theoretical simulations, we used a combination of the finite-difference time-domain (FDTD) and surface integral equation (SIE)[27] methods and an optimized T-matrix code.[28]

We show that even after surface and orientation averaging, and taking into account the Raman Stokes shift, the agreement between experimental and simulated data is still unsatisfactory for PRs below the laser excitation wavelength. In contradiction with common practices for the optimization of the SERS response, the tuning of the AuNR aspect ratio to the excitation laser wavelength seems unimportant. In particular, for PRs above the laser excitation wavelength both experimental measurements and EM simulations show a weak flattened dependence of the EF on the aspect ratio or on the PR wavelength. For PR wavelengths below the laser wavelength, the simulated EFs decrease by an order of magnitude, whereas the experimental EFs vary insignificantly. By contrast, small variations in AuNR shape can be the right recipe to increase the SERS response even under off-resonance conditions. Such a strategy is demonstrated here by overgrowing the initial AuNRs to produce a dumbbell morphology, which increases the SERS response more effectively than does resonance tuning. We also show that our relatively large randomly oriented AuNRs produce a strong SERS background whose spectral properties correlate with the extinction spectra. This background can be related to plasmonically enhanced photoluminescence (PL), similar to what was shown previously for single nanorods.[29,30] Another possible explanation is the elastic scattering of the very weak and broad laser background by randomly oriented AuNRs.

EXPERIMENTAL AND THEORETICAL METHODS

Materials. All chemicals were obtained from commercial suppliers and were used without additional purification. Hexadecyltrimethylammonium bromide (CTAB, >98.0%), hexadecyltrimethylammonium chloride (CTAC; 25% water solution), sodium oleate (NaOL, technical grade; >82% fatty acid), L-ascorbic acid (AA, >99.9%), 4-nitrothiophenol (1,4-nitrobenzenethiol, NBT), hydrochloric acid (HCl, 37 wt % in water), sodium borohydride ($NaBH_4$, 99%), and 1,4-dithiothreitol (DTT) were all purchased from Sigma−Aldrich. Hydrogen tetrachloroaurate trihydrate ($HAuCl_4 \cdot 3H_2O$) and silver nitrate ($AgNO_3$, >99%) were purchased from Alfa Aesar.

AuNR Synthesis and Functionalization. Seeds were prepared by adding 0.25 mL of 10 mM $HAuCl_4$ to 10 mL of aqueous 0.1 M CTAB. This was followed by adding 0.6 mL of a 10 mM sodium borohydride solution. The seed solution was aged at room temperature for 90 min before use. For preparing the growth solution, 7.0 g of CTAB and 1.234 g of NaOL were dissolved in 250 mL of water. Then, 18 mL of 4 mM $AgNO_3$ was added. The mixture was kept undisturbed at room temperature for 15 min, after which 250 mL of 1 mM $HAuCl_4$ was added. After 90 min of stirring, 2.1 mL of HCl (37 wt %) was added, and after another 15 min 1.25 mL of 64 mM ascorbic acid and 0.1 mL of the seed solution were added. The resultant mixture was left undisturbed at 30 °C for 48 h for AuNR growth. This protocol yielded AuNRs with a longitudinal plasmon peak at 900−925 nm. AuNRs were sedimented by centrifugation at 10 000×*g* for 15 min and were resuspended in 100 mM CTAB.

AuNRs with different aspect ratios and plasmon peaks were obtained by the controllable etching of the initial CTAB-coated particles.[26] To this end, 10 mL of AuNR stock solution was mixed with 25, 50, 75, 100, 112.5, 125, 150, and 175 μL of 10 mM $HAuCl_4$ and the mixture was left to etch overnight. To avoid possible loss of AuNRs and to prevent their partial aggregation, the resulting AuNR samples with different plasmon bands (700−900 nm, Set 1 samples) were used without centrifugation and washing steps.

AuNRs with dumbbell morphology were synthesized by the protocol from the paper.[31] Briefly, the growth solution was made by adding 0.5 mL of 10 mM $HAuCl_4$ and 0.1 mL of 100 mM AA to 10 mL of 100 mM CTAB. The washed AuNRs and the growth solution were mixed 1:1 and were incubated at 30 °C for 24 h. The resulting particles were used without washing.

The cigarlike AuNRs and dumbbell AuNRs were functionalized with NBT by the addition of 100 μL of 2 mM NBT in ethanol. After incubation for 2 h, NBT-coated AuNRs were used without any centrifugation and washing steps to prevent a partial aggregation and the particle loss.

For measurements with Renishaw InVia Raman microscope, we also prepared an independent Set 2 of eight AuNR-650−AuNR-925 samples by using the same synthesis and

https://dx.doi.org/10.1021/acs.jpcc.0c00991
J. Phys. Chem. C 2020, 124, 10647−10658

functionalization steps as for Set 1. The only difference between Set 1 and Set 2 samples was the centrifugation (10 000×*g* for 15 min) and washing (10 mM CTAC) steps after etching and functionalization. We will show that this difference between synthesis protocols does not affect our main conclusions.

Atomic Absorption Spectroscopy (AAS). For quantifying the number of gold nanorods in etched samples, the gold concentration was measured by AAS method with a Dual Atomizer Zeeman AA iCE 3500 spectrophotometer (Thermo Scientific Inc., U.S.A.). To this end, 0.5 mL of aqua regia was added to 1 mL of each AuNR sample and then 3.5 mL of water was added to the dissolved particles before measurements (method 1). Alternatively, the AuNR sample was centrifuged, the pellet was dissolved in 0.5 mL of aqua regia, and then 4.5 mL of water was added to the dissolved particles (method 2). The number of gold nanorods was calculated as a ratio of the mass−volume gold concentration to the average mass of a single nanorod as determined by TEM analysis (Section S8).

Quantifying the AuNR Concentration by UV−vis Spectrophotometry. For quantifying the AuNR concentration, two variants of UV−vis spectrophotometry were used (Section S9). In the first one, the plasmonic peak extinction was measured and correlated with T-matrix calculations for polydisperse ensembles of AuNRs derived from TEM analysis. The second variant is based on the measurements of AuNR absorption in the 400−450 nm spectral range. The 400−450 nm absorption is mainly determined by the total gold concentration[32] rather than by the particular particle shape and structure.[33] The number of gold nanorods was found by combination of the absorption measurements with T-matrix calculations of the molar decadic extinction coefficient (Section S9).

Quantifying the NBT Concentration. A 5 mL sample of AuNRs with adsorbed NBT molecules was washed three times in 5 mM CTAC and then additionally in water. The washed AuNRs were centrifuged and incubated with 500 μL of 1 M DTT for 24 h. Then the particles were centrifuged and the NBT concentration in supernatant was measured spectrophotometrically (Section S10) in a special 1 cm cuvette of a small volume (the cuvette width was 3 mm).

SERS measurements. SERS spectra of AuNRs with adsorbed NBT were measured by using two types of Raman devices operated at 785 nm. First, SERS spectra were measured with a Peak Seeker Pro 785 Raman spectrometer (Ocean Optics) in 1 cm path length quartz cuvettes (laser power, 30 mW; acquisition interval, 10 s). The inner filter effect was excluded by focusing the laser near the front cuvette wall. Second, a 10 μL drop of each sample was placed onto the quartz substrate and SERS spectra were measured with a confocal Renishaw InVia Raman microscope (objective, 50×; wavelength, 785 nm; laser power, 7 μW; integration time, 10 s). The laser beam was focused on the sample's top.

EM Simulations. For all EM simulations, the surrounding medium was water with a refractive index of 1.334, and the optical constants of Au were taken from Jonson and Christy.[34]

FDTD Simulations. The field distributions around nanorods were simulated with Lumerical FDTD Solutions software for AuNRs modeled as cylinders with semispherical ends (cigarlike particles). The size and the aspect ratio of the particles were taken from TEM images. The FDTD simulation volume was a 128 × 48 × 48 nm parallelepiped with a uniform mesh of 0.2 nm spacing. The incident plane wave at 785 nm was polarized along the symmetry axis. A 3D field monitor was used to collect the EM field distribution.

T-matrix Simulations. T-matrix simulations of AuNR extinction spectra with ensemble and orientation averaging were made as described in SI (Section S2; see also ref 35). T-matrix simulations of the SERS EFs for spheroidal particles were done with publicly available codes (SMARTIES)[28] with $n = 15$ multipoles, all m's $[-(2n + 1) \leq m \leq 2n + 1]$, and 80 points for the theta-quadrature. Local fields at the particle surface $|E_L|$ and $|E_R|$ were calculated for the laser excitation and Raman wavelengths, respectively. Surface-averaged quantities were calculated by using a rectangular quadrature of 360° θ and analytical averaging for azimuth φ. For orientation averaging, the calculated data were averaged over 400 incident directions (20 points Gaussian quadrature for θ, and 20 points rectangular quadrature for φ) and over two orthogonal polarizations. The polarization effect for the surface and orientation averaged EF = $\langle\langle |E_L|^2 |E_R|^2\rangle_S\rangle$ involves cross-terms, and this was taken into consideration.

SIE Calculations. The surface-integral equation formalism[36] was used to calculate the (full-wave solution) electric field on the surface of gold nanocigars. We have used an implementation specially developed (and tested) for plasmonic and metallic nanoparticles.[27] The mesh average element size is kept constant resulting in 1320 surface elements (triangles) for an aspect ratio of 2, increasing to 3984 elements for an aspect ratio of 6 (diameter kept constant at 26 nm). The wavelength dielectric function of gold is taken from Johnson and Christy[34] and the embedding medium (water) has a refractive index of 1.334. For a given incident excitation, the fields were calculated at both the laser excitation and Raman wavelengths, then surface-averaged to deduce $\langle |E_L|^2 |E_R|^2\rangle_S$. Finally, the orientation-averaged EFs were obtained by averaging the results over 1000 random incident direction and polarization. Note that the SIE interaction matrix is independent of incident excitation, and solving the linear system for 1000 excitations is not much more costly than for one. This method was validated for spheroidal nanoparticles against the T-matrix results.

RESULTS AND DISCUSSION

AuNR Synthesis by Controllable Etching. To best examine the dependence of the SERS EF on the plasmonic properties of gold nanorods, one should prepare samples with identical particle concentration and morphology but with different particle axial ratios. Although the existing protocols for AuNR synthesis allow the PR to be tuned over the vis−NIR spectral band, some important structural details of the samples obtained by independent syntheses can be very different, thus making the comparison of SERS data less reliable. First, the yield of nanorods in a typical protocol may vary from 80% to 99%. Second, the diameter of the particles may vary together with the plasmon peak position. Finally, nanorods from different batches can have different shapes such as cigars, dogbones, or dumbbells. All these factors can strongly affect the SERS signal of the adsorbed Raman molecules. To overcome these drawbacks, we decided to use a single batch of the initial cigarlike nanorods with the maximal aspect ratio and then obtain samples with a smaller aspect ratio by the controllable etching of the initial nanorod ends. From TEM analysis, the initial AuNRs were of average thickness $d = 25.4 \pm 1.2$ nm, length $L = 109.5 \pm 5.8$ nm, and aspect ratio AR = 4.3 ± 0.34 (Set 1), and their longitudinal plasmon peak was at 900 nm (Figure 1 and SI Figure S1). A high ratio between

https://dx.doi.org/10.1021/acs.jpcc.0c00991
J. Phys. Chem. C 2020, 124, 10647−10658

major and minor extinction peaks (>6) is indicative of a low amount of impurities in a sample.[37]

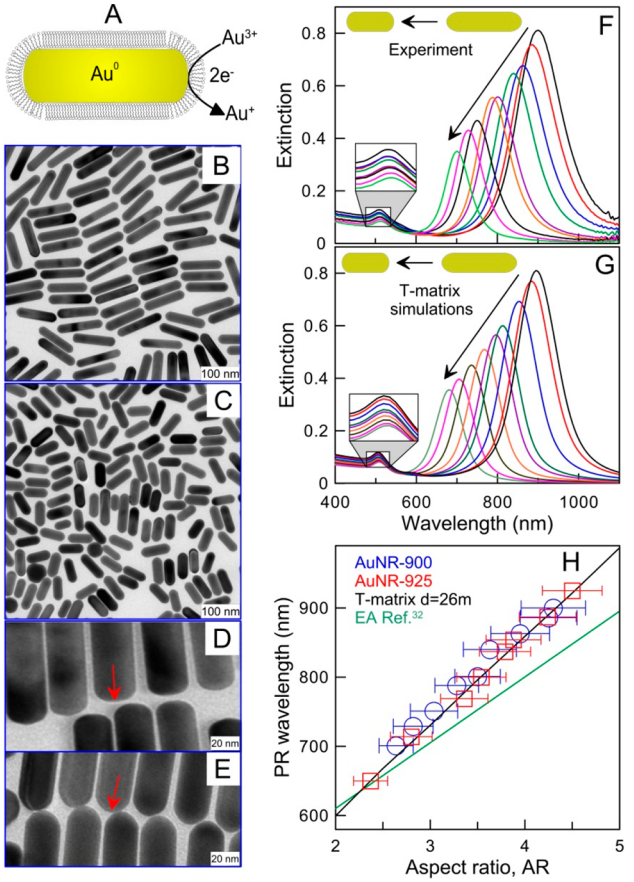

Figure 1. (A) Selective etching of AuNRs with the Au−CTAB complex (A). TEM images of the initial (B) and final (etched) nanorods (C) with longitudinal PR wavelengths at 900 and 700 nm, respectively. The red arrows in panels (D) and (E) show TEM images of the initial flat tips of as-prepared AuNRs and those after etching with a minimal amount of the Au−CTAB complex. (F) Extinction spectra of the initial and etched nanorods obtained by the addition of 0−175 μL of $HAuCl_4$ to 10 mL of the initial AuNRs. (G) Simulated extinction spectra of polydisperse ensembles of AuNRs with a constant thickness of 26 nm and with aspect ratio distributions derived from TEM images (for details, see SI, Section S2). (H) Dependence of the longitudinal PR on the TEM-measured aspect ratio of the nanorods. Two independent sets of experimental data are shown: one for AuNR-900 (blue circles) and the other for AuNR-925 (red squares). Horizontal bars display standard deviations of aspect ratios derived from TEM images. Shown also are the T-matrix simulation plot (the constant nanorod diameter of the polydisperse ensembles is 26 nm, black line) and the dipolar Electrostatics Approximation[38] for monodisperse Au spheroids (green line).

Next, we etched the initial nanorod sample by the addition of various amounts of $HAuCl_4$ to the nanoparticles dispersed in 0.1 M CTAB. After the addition of $HAuCl_4$, an Au^{3+}−CTAB complex was immediately formed, as evidenced by the bright yellow color of the solution. Then, the gold rods were slowly dissolved by Au^{3+} ions (within 24 h), which resulted in a blue-shifted AuNR PR. Note that the etching takes place only in the presence of CTAB, because CTAB changes the reduction potential of Au^{3+} upon complexion.[25] Because of the different densities of the CTAB bilayers on the flat slides and curved tips, the oxidation of the AuNRs with the Au−CTAB complex led to a shortening of the rods with no change in width (Figure 1A). With an increased amount of added $HAuCl_4$, the TEM images show an almost equal average 26 nm width of the AuNRs, while the average length decreased from 110 nm (Figure 1B) to 68 nm (Figure 1C; more information in SI, Table S1). The progressive shortening of the rods led, as expected, to a blue shift of the longitudinal PR from 900 to 700 nm and to a decrease in the extinction peak magnitude (Figure 1F). The reason for the latter is the decrease in the extinction cross section of the etched rods, rather than a change in the particle concentration, which was kept constant in the etching experiments. Figure 1G shows the simulated extinction spectra of the AuNRs with a constant thickness of 26 nm and the normal aspect ratio distributions derived from the TEM images. The simulated spectra were normalized according to eq S13 (SI, Section S2). There is good agreement between experimental and theoretical spectra for the position of the extinction maxima, their relative decrease in peak magnitude, and the spectral width in terms of fwhm. Note that eq S12 implies constant number concentration of AuNRs in etched samples. Therefore, good agreement between the measured and calculated extinction peaks confirms our assumption that the etching process keeps the number concentration constant, whereas the mass−volume concentration of gold nanoparticles decreases progressively.

For simulations, we used a constant relative standard deviation of the aspect ratio distributions $\Delta AR/AR_{av} = 0.06$. With this STD, the simulated spectra are less broadened than the measured ones for the initial etching steps. However, for the final etched particles the aspect ratio STD should be increased slightly to fit the experimental fwhm. In any case, quite small fitting parameter $\Delta AR/AR_{av} = 0.06$ is another sign of the high quality of the samples.

For measurements with the Renishaw inVia Raman microscope, we independently fabricated AuNRs with a length of 115.6 ± 6.0 nm, a thickness of 25.4 ± 1.3 nm, an aspect ratio AR = 4.76 ± 0.33, and a PR at 925 nm (Set 2). The particles were then etched to produce a set of nanorods with plasmon peaks of 925−655 nm. The TEM images and extinction spectra are given in the SI (Figure S2).

Figure 1H shows the experimental relationship between the longitudinal PR wavelength and the TEM-derived aspect ratio of the nanorods. The experimental data are presented for two independent sets of synthesis, etching, and characterization (AuNR-900 and AuNR-925). The data are in good agreement with the T-matrix simulations for AuNRs of 26 nm width. Note that the simpler dipolar approximation[38] gives worse agreement with experimental points, because the shape of AuNRs differs from that of ellipsoids and because the particle size is somewhat larger than the upper limit of the Rayleigh approximation,[39] which was applied by Gans to randomly oriented ellipsoids.[40]

Finally, we noticed an important morphological difference between initial and etched nanorods. After the AuNRs were etched with a minimal amount of $HAuCl_4$, the axial ratio remained almost unchanged, but the PR was blue-shifted by 20 nm. This small but reproducible effect can be explained by a change in the shape of the rod cap from a flatter morphology (Figure 1D) to a more curved one after the very initial etching step (Figure 1E). Such an effect blue-shifts the main peak.[35,41] Following this initial step, the end-cap shape no longer changes

https://dx.doi.org/10.1021/acs.jpcc.0c00991
J. Phys. Chem. C 2020, 124, 10647−10658

during progressive etching, and the particles can be well described by the cigarlike model, regardless of their length.

In summary, we have obtained two sets of eight samples of nanorods that had identical morphologies, concentrations of particles, and amounts of byproducts but differed only in the position of the longitudinal PR (SI, Tables S1 and S2). The PRs of these samples span a wide range around an excitation wavelength of 785 nm.

SERS Measurements. The fabricated AuNRs were further functionalized with NBT molecules, and SERS spectra were measured in the backscattering mode upon 785 nm excitation in a cuvette.

Figure 2A shows the SERS spectra of NBT adsorbed on AuNRs with different PRs. In agreement with our previous

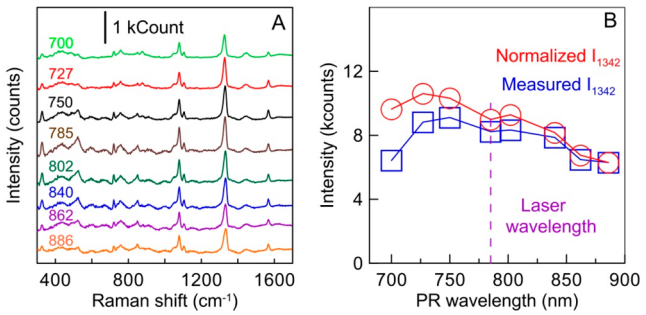

Figure 2. (A) SERS spectra of NBT adsorbed on AuNR-900 nanorods with different longitudinal PRs. Measurements were made with a Peak Seeker Pro 785 Raman spectrometer. The background was subtracted by using a polynomial fit. (B) Dependences of the measured and normalized (to the AuNR surface area) SERS intensities at 1342 cm^{-1} on the PR wavelength of the AuNRs.

measurements,[42] the SERS spectra for all samples are dominated by nitrobenzene peaks associated with specific vibrations of the chemical groups between 854 and 1569 cm^{-1}. It should be stressed that we obtained comparable intensities of the characteristic peaks for all samples, regardless of the plasmonic peak positions of the AuNRs. For example, for AuNR-727 (blue-shifted), AuNRs-788 (on-resonance), and AuNR-886 (red-shifted), the intensities of the major Raman band at 1342 cm^{-1} were 882, 823, and 630 counts, respectively. This comes as a great surprise, because the current electromagnetic theories of SERS[24] predict much more variation in the SERS intensity under plasmon detuning (see below). This point contradicts common belief and deserves a special discussion. Note that even a small fraction of aggregated particles could have affected the measured SERS signal strongly;[43] that is why we excluded any centrifugation and washing steps during synthesis and functionalization of AuNRs with NBT (Set 1).

A typical figure of merit of the SERS response is the fundamental EF, which is calculated as the ratio between SERS and Raman intensities normalized to the corresponding numbers of excited molecules.[44] We use the most intense Raman peak at 1342 cm^{-1} to compare the SERS responses from different nanorods. Typically, an accurate evaluation of the number of excited SERS molecules is quite challenging. But in our experiments, all conditions and factors except particle length (and, therefore, particle surface area) were identical for all samples. This means that the number of adsorbed molecules should be proportional to the nanoparticle surface area. Therefore, for a comparative evaluation we can normalize the SERS intensities to the surface area of the particles (determined from the TEM data). Figure 2B shows the dependence of the normalized SERS intensity (circles) on the PR wavelength. The highest SERS response was observed for AuNRs with a slightly blue-shifted PR, as compared to the laser wavelength. However, in general, all variations in the normalized intensity are very low, less than two times between the highest and lowest signals. A similar conclusion can be derived from the directly measured non-normalized data. In our recent work,[42] we showed that NBT molecules are predominantly adsorbed on the AuNR ends. Taking into account the constant concentration of rods in all samples and the same morphology of the AuNR ends, we can assume a constant or comparable concentration of the reporter molecules in all samples, in agreement with data by Sivapalan et al.[17] In this case, no normalization is required and such intensities are presented in Figure 2B (squares). Again, we arrive at the same important conclusion: the sensitivity of the SERS response to PR detuning is quite weak.

Of course, the above conclusion holds only for a moderate detuning of ±100 nm. For extreme cases with very strong PR detuning, one should expect a notable decrease in SERS response. Indeed, for gold nanospheres (PR, about 520 nm) and long nanorods with an aspect ratio of 7 and a PR of ~1065 nm, we observed very weak peaks at 1342 cm^{-1}, 20 counts for spheres, and 40 counts for rods (SI, Figure S3). Such small peaks cannot be explained by differences in the concentration of particles or excited molecules. Therefore, we attribute these small intensities to strong plasmonic detuning.

To confirm that our experimental results were in no way affected by the specific features of the initial AuNR samples before and after etching and by the measurement scheme in a cuvette, we conducted an additional experiment with an independent starting sample, AuNR-925, and with another Raman spectrometer. Specifically, we functionalized eight AuNR-650−AuNR-925 samples with NBT as discussed above and conducted SERS measurements with a colloid drop by using a Renishaw inVia microscope (Figure 3). In agreement with the data of Figure 2, the SERS spectra of the AuNRs with PRs between 700 and 880 nm are quite similar. A notable decrease in the SERS signal is observed only for samples with extreme PRs at 650 and 925 nm.

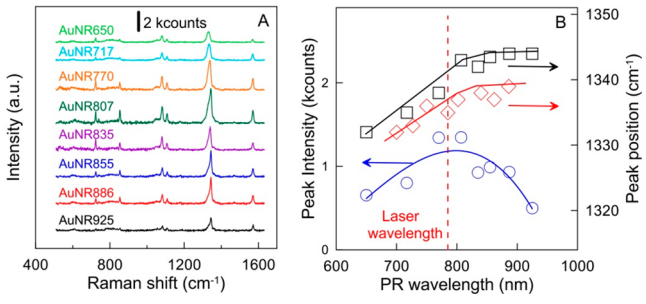

Figure 3. (A) SERS spectra of NBT adsorbed on the AuNR-925-derived nanorods with different longitudinal PRs (indicated on the plot). Measurements were made with a Renishaw inVia Raman spectrometer. The background was subtracted by using a polynomial fit. (B) Dependences of the SERS intensities at 1342 cm^{-1} on the PR wavelength of the AuNRs. The peaks intensities are normalized to the particle surface. Black squares show a weak dependence of the main SERS peak position on the PR wavelength when greater than the laser wavelength. Red rhombs show similar data for AuNR-900 (Figure 2).

https://dx.doi.org/10.1021/acs.jpcc.0c00991
J. Phys. Chem. C 2020, 124, 10647−10658

The solid blue line in Figure 3B is a polynomial fit as a guide to the eye. Because of the notable spreading of the experimental points in the PR range of 700−850 nm, we cannot derive the optimal excitation wavelength and its relationship to the PR wavelength with sufficient accuracy. In fact, all AuNRs within the 700−850 nm band again demonstrate similar SERS responses.

The experimental data in Figure 3B (black squares) show a weak dependence of the main SERS peak position at 1340 cm^{-1} on the PR wavelength of AuNRs. This peak corresponds to a symmetric stretching vibration of the NO_2 group. Note that for other peaks, the change in their spectral position with decreasing aspect ratio is about 2.5 cm^{-1}, whereas the shift of 1340 cm^{-1} is 4 times higher, that is, about 10 cm^{-1}. A similar notable shift of the main peak was also observed for AuNR-900 (Figure 3B, red rhombs). The difference between black and red curves in Figure 3B could be related, at least in part, to the different Raman spectrometers used for measurements with Set 1 and Set 2 AuNRs.

A possible explanation for similar trends of both red and black curves in Figure 3B can be as follows. The NBT sample in our experiments could be a mixture of the 1,2- and 1,4-NBT isomers.[45] It has been shown recently[46] that for various plasmonic SERS tags (Au nanorods, Au nanostars, and silica/Au nanoshells), the symmetric NO_2 stretching mode of the surface-adsorbed NBT molecules appears as a Raman line at 1343 cm^{-1} and a shoulder at 1331 cm^{-1}. For tags with NBT molecules embedded in a 1 nm gap between Au core (spheres or rods) and Au shell, the SERS spectra showed a downshift of the symmetric NO_2 stretching of *p*-NBT from 1343 to 1300 cm^{-1}, whereas the line for *o*-NBT remained unchanged at 1331 cm^{-1}. In fact, the broadened peak near 1340 cm^{-1} was a doublet with two closely spaced peaks that could be resolved only with gap-enhanced Raman tags. The etching of the as-prepared AuNRs possibly led to small changes in the surface morphology of the etched rods, as compared to the initial ones. These changes could have modified slightly the local environment of the Raman molecules and their preferential orientation, thus causing changes in the relative intensity of the doublet peaks. This could have resulted in an apparent shift of the broadened peak. It should be noted, however, that the subtle morphological difference in etched AuNRs did not affect SERS response. Therefore, we believe that the "chemical" contribution does not change the measured SERS response for different samples and does not affect our main conclusions.

In summary, we have observed a weak dependence of the SERS signal on the PR position in a narrow but notable wavelength range (650−900 nm). We will show further that this result is not fully consistent with estimates based on electromagnetic simulations of the EF, which account for the Raman shift (i.e., beyond the $|E(\omega_L)|^4$ approximation), the averaging on the particle surface, and random particle orientations.

Inner Filter Effect and PL Background. Given the unexpected data of Figures 2 and 3, we first examined two important effects that could affect SERS measurements in AuNR colloids. One is the "inner filter" effect,[47] caused by the extinction of light traveling from its source to the exciting particle or molecule and by the extinction of emitted light traveling from the particle to the detector. By contrast with single-particle measurements, the inner filter effect can strongly affect the SERS spectra under on- and off-resonance conditions, when the difference in light absorption can be significant and all other conditions are supposed to be equal. Fortunately, there exists a simple concentration test with sequential dilutions. Figure S4A shows SERS spectra similar to those in Figure 2A after a 1:5 dilution to check whether the inner filter effect should be corrected. Figure S4B gives a quantitative measure in terms of the ratio between SERS intensities at 1342 cm^{-1} for the initial and diluted samples. As expected, the dilution results in a 5-fold decrease in the intensity and in a deterioration of the signal-to-noise ratio. This means that our SERS measurements and conclusions are not distorted by the inner filter effect.

The other important effect is the contribution of the PL background (Bg) to the recorded SERS spectra.[18,21] The enhancement of PL by localized plasmons is well accepted;[29,30] however, the interpretation of the observed emission as PL versus electronic Raman scattering is still debated.[21,48] Nevertheless, the presence of a spectral-dependent Bg in our nonbaseline-corrected SERS spectra is clear (Figure 4). The correction of the measured SERS spectra for the Bg and PL contributions is not a trivial problem, and it was addressed in detail recently[21] by using single AuNR SERS and light scattering measurements.

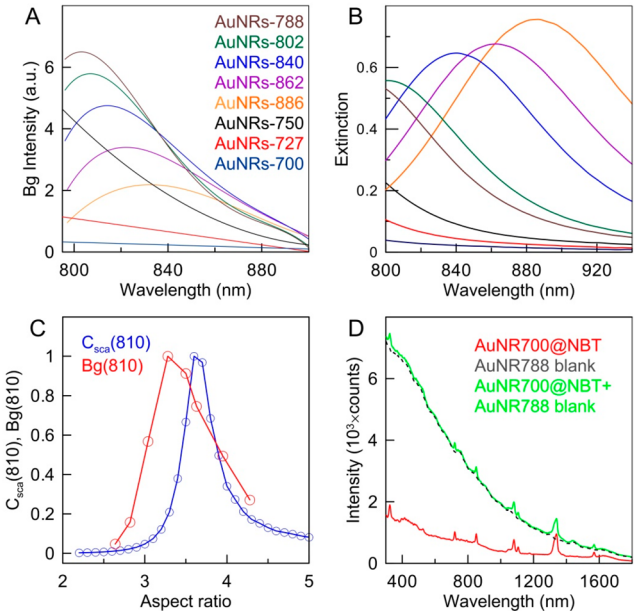

Figure 4. SERS background after polynomial fit (A) and measured extinction spectra (B) of AuNR@NBT with PRs in the range 700−886 nm. Panel C shows the normalized calculated scattering cross section and the Bg intensity at 810 nm as a function of the AuNR aspect ratio. Panel D displays the SERS spectra of NBT adsorbed on AuNRs with a PR of 700 nm (red curve, weak Bg), SERS spectra of naked 788 nm AuNRs (dashed curve, only Bg is seen), and a mixture of the two types of nanoparticles (green curve, strong Bg with SERS peaks at the same positions).

Figure 4A shows the polynomial fits of the SERS Bg spectra, whose shape resembles the PL spectra of single AuNRs.[21,29,30] Several important notes are in order here. First, the intensity of the Bg spectra is maximal for the AuNR-788 sample, whose PR corresponds to the on-resonance excitation at the laser wavelength. For all other off-resonance samples, we observed smaller Bg intensities. Second, the wavelength peaks of the Bg spectra correlate clearly with the PR extinction wavelengths of the AuNRs. Indeed, a close comparison of the Bg and

https://dx.doi.org/10.1021/acs.jpcc.0c00991
J. Phys. Chem. C 2020, 124, 10647−10658

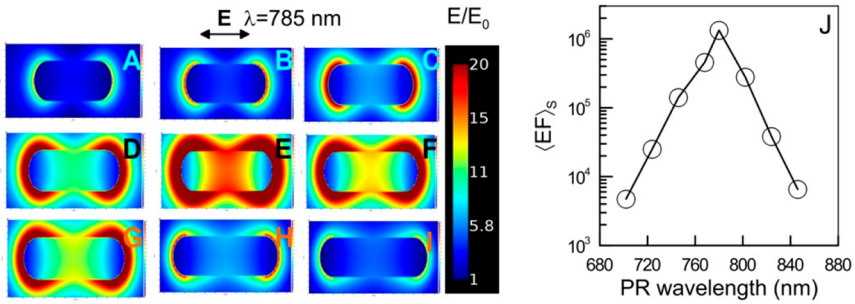

Figure 5. FDTD-simulated 2D field distributions around cigarlike AuNRs with a thickness of 26 nm and a length of 74 (A), 78 (B), 82 (C), 86 (D), 90 (E), 94 (F), 98 (G), 102 (H), and 106 nm (I). Panel (J) shows the simulated surface-averaged enhancement factor $EF_S = \langle |\mathbf{E}_{loc}|^4 \rangle_S$ as a function of the PR wavelength of the AuNRs for longitudinal laser excitation at 785 nm.

extinction spectra (Figure 4B) demonstrates similar behavior in the dependence of the spectral peaks on the aspect ratio. On the basis of these observations and with account taken of the published data (see, e.g., refs 29, 30, and 48 and references therein), one could attribute the Bg of the spectra in Figures 4A, at least its major portion, to the PL contribution. It can be confirmed that the Bg signal comes from AuNRs, rather than from NBT. Indeed, the measurements of SERS spectra from as-prepared nonfunctionalized AuNRs show the same Bg spectra as in Figure 4A but without the Raman lines from NBT molecules (see dashed line in Figure 4D).

Another explanation of the Bg origin could be the elastic light scattering of weak laser fluorescence by gold nanorods, because our Raman spectrometer works in backscattering fiber optic geometry without a band stop filter (see Figure S2). Figure 4C shows the calculated elastic light scattering cross sections for a wavelength of 810 nm as a function of the AuNR aspect ratio. The calculated data are normalized to the peak value at an aspect ratio of about 3.6. One can see a close correlation between the scattering cross section plot (blue line) and the measured normalized Bg_{810} intensity (red line) as a function of the TEM-derived aspect ratios. This correlation, however, does not exclude the explanation of the Bg origin as the PL from excited AuNRs. Indeed, Len et al.[21] showed that far-field scattering coincides with the integrated near-field intensity, which is closely related to excited PL spectra.

Because the Bg intensity depends strongly on the PR of nanorods at a given laser wavelength, it is important to find out how the Bg affects the intensity of the detected Raman lines. To this end, we measured the spectra for three samples: gold nanorods with a PR at 700 nm and adsorbed NBT molecules (Raman lines and weak Bg, red spectrum), bare nanorods with a PR at 788 nm (no Raman lines, strong Bg, black dashed curve), and mixtures of the two samples with equal particle concentrations (green spectrum with peaks and strong Bg). The three measured spectra shown in Figure 4D demonstrate an additive effect of the Bg without any significant nonlinear effects of PL on the intensity of the Raman line.

In summary, we have confirmed that both the inner-filter and Bg mechanisms do not affect our main finding. Namely, the SERS intensity from AuNR colloids with PRs of 650−925 nm exhibits a weak variation for 785 nm excitation. We now proceed to discuss electromagnetic simulations.

Simulations of the Near-Field Enhancement. *FDTD Simulations of the Near-Field Distribution and the Surface-Averaged EF at a Fixed Longitudinal Excitation.* In its simplest form, the SERS EF can be estimated as the product of the local intensity enhancements for the laser and Raman frequencies.[24] This local SERS EF should be averaged over the particle surface and for colloids should be averaged over random particle orientations. A comprehensive analysis of the physical conditions behind the four-power approximation $|\mathbf{E}_{loc}(\omega_L)|^2|\mathbf{E}_{loc}(\omega_R)|^2 \sim |\mathbf{E}_{loc}(\omega_L)|^4$ can be found in the book.[24] In short, this approximation is applicable under the following conditions: (1) the geometry of measurements is back-scattering, (2) the excitation and detection polarizations are collinear, and (3) the surface-selective factor is close to 1 (see eq 4.73 in ref 24). It should be stressed that this approach gives a simplified treatment of the directional radiation EF[24] by replacing it with the local intensity enhancement at the Raman frequency. Besides, it also ignores any local properties of Raman molecules, including their surface distribution and orientation.

Using FDTD Lumerical Solution software, we calculated the field distribution around the cigarlike AuNRs in the case of longitudinal excitation. Figure 5A−I shows the local near-field distribution in a two-dimensional equatorial plane that contains the exciting field vector and the nanorod symmetry axis. The local electromagnetic field depends strongly on the geometrical parameters of the AuNRs. As expected, the greatest local field enhancement was observed when the PR coincided with the excitation wavelength. In our case, this was observed for an AuNR length of 90 nm (Figure 5E). Accordingly, in contrast to the experimental observations in Figures 2 and 3, the electromagnetic EF changed substantially when the PR was detuned from the laser wavelength (Figure 5J). In particular, the PR detuning from 785 to 700 nm resulted in a two-orders-of-magnitude decrease in the predicted SERS intensity. However, such a strong dependence was not observed in actual experiments (Figures 2 and 3). Thus, there is a major disagreement between the FDTD simulation data and the experimental measurements of the spectral-dependent SERS responses from the AuNRs.

T-Matrix and SIE Simulations of the Averaged EF for Spheroidal Particles. The above FDTD calculations (Figure 5J) were done for a fixed longitudinal orientation of the nanorods relative to the excited electric field polarization and within the fourth-power approximation $EF_S = \langle |\mathbf{E}_{loc}(\omega_L)|^4 \rangle_S$, which both result in overestimated EFs. To include the random orientations in our simulations, we adopt the SIE method.[27] Our goal is to calculate the averaged SERS EF

$$\langle EF_S \rangle = \left\langle \frac{1}{S} \int |\mathbf{E}_{loc}(\omega_L)|^2 |\mathbf{E}_{loc}(\omega_R)|^2 dS \right\rangle = \langle \langle |\mathbf{E}_{loc}(\omega_L)|^2 |\mathbf{E}_{loc}(\omega_R)|^2 \rangle_S \rangle \quad (1)$$

https://dx.doi.org/10.1021/acs.jpcc.0c00991
J. Phys. Chem. C 2020, 124, 10647−10658

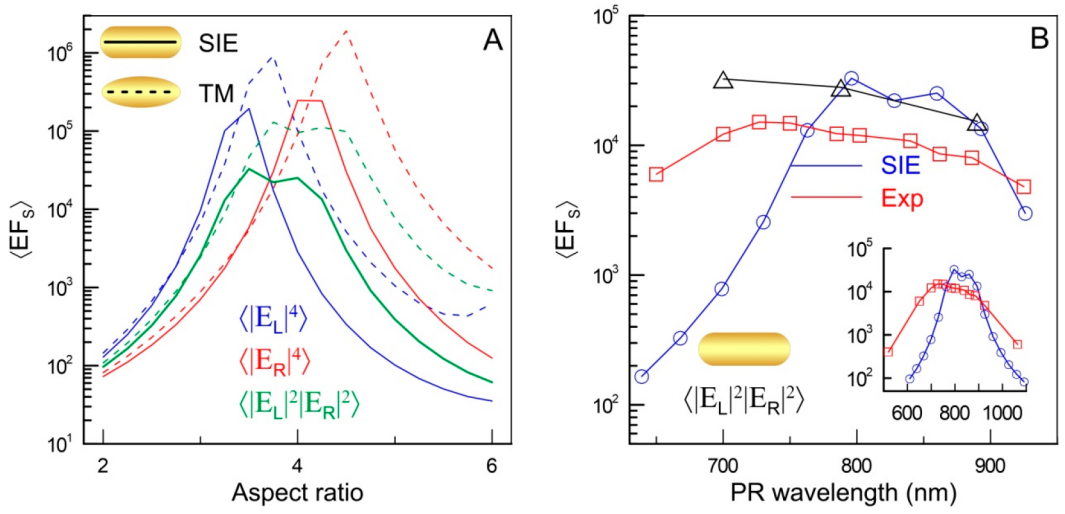

Figure 6. (A) Orientation- and surface-averaged local fields for the laser wavelength ($\langle |E_L|^4 \rangle$, blue curves), the Raman-shifted wavelength ($\langle |E_R|^4 \rangle$, red curves), and the SERS EF $\langle |E_L|^2|E_R|^2 \rangle$, green curves) as a function of the aspect ratio. Calculation by the T-matrix method for nanospheroids (dashed lines) and by the SIE method for nanocigars (solid lines). (B) Experimental (red squares) and SIE-calculated (blue circles) dependences of the surface- and orientation-averaged SERS EF $\langle |E_L|^2|E_R|^2 \rangle$ on the PR wavelength. The black triangles show independent measurements for Set 3 of AuNRs with quantifying the number of gold nanorods and the number of NBT molecules adsorbed on one nanorod (Sections S8–S10). The inset shows an enlarged spectral range that includes two experimental points for spheres and long AuNRs. Particle diameter is kept constant at 26 nm.

where the outer angular brackets designate the averaging over orientations of particles; the inner angular brackets with the subscript S stand for the averaging over the particle surface; and ω_L and ω_R are the excitation laser and Raman-shifted angular frequencies of the incident laser light, respectively. Because of the strong spectral dependence of the local field intensity on the excitation frequency, we do not simplify eq 1 by using the approximation $\omega_R \simeq \omega_L$, which leads to the known four-power law EF $\sim |\mathbf{E}_{loc}(\omega_L)|^4$. To further test that the results are not specific to the spheroidal model, we did additional simulations with cigarlike AuNRs. The local fields were calculated by the surface integral equation (SIE) method,[27] and then surface and orientation averaging was done with eq 1.

Figure 6A shows the surface- and orientation-averaged local fields $\langle |E_{loc}|^4 \rangle$ for the laser and Raman-shifted wavelengths ω_L and ω_R, respectively, as a function of the aspect ratio of nanospheroids (T-matrix calculations) and nanocigars (SIE calculations). There is a small shift in the peak position between cigars and spheroids, as also observed previously.[49] Because of the resonance behavior of the $\langle |E_L|^4 \rangle$ and $\langle |E_R|^4 \rangle$ quantities and because of the notable difference in their peak position, the fourth-power law strongly overestimates the EF, as compared with the SERS EF calculated with eq 1. The average cigar EFs are also reduced, as compared to those of spheroids because of the reduced curvature at the tip. There is a flat portion of the full EF $\langle |E_L|^2|E_R|^2 \rangle$ as a function of the aspect ratio (Figure 6A, green curves) for PR wavelengths between 800 and 900 nm (Figure 6B, blue curves). That is what we observed in our measurements (Figure 6B, red curves) for AuNRs whose PR was above the excitation wavelength. To the best of our knowledge, Figure 6B gives the first experimental and theoretical demonstration of an almost constant electromagnetic contribution to the average SERS EF for a plasmonic system with a variable PR (785–925 nm). With increasing AuNR aspect ratio and PR wavelength, the predicted SERS EF starts to decrease, which is in agreement with the experimental data for long nanorods (Figure 3 and SI Figure S3, for AuNRs with an aspect ratio of about 7 and a PR of 1065 nm). However, for aspect ratios smaller than 3.5 or, equivalently, for PRs below the excitation wavelength, the simulated EFs decrease by almost 2 orders of magnitude, in drastic contrast with the experimental data.

Yet another important conclusion is that the widely used zero-shift four-power law gives incorrect estimates of the SERS EFs, even when surface and orientation averaging is taken into account (EF = $\langle \langle |\mathbf{E}_{loc}(\omega_L)|^4 \rangle_S \rangle$). The calculated EF dependences on the PR wavelength have a narrow-width peak centered at the laser excitation wavelength (blue plots in Figure 6A) or at the Raman-shifted wavelength, corresponding to $\langle \langle |\mathbf{E}_{loc}(\omega_R)|^4 \rangle_S \rangle$ (red plots in Figure 6A). When the full eq 1 is used for simulations, the integrand product of the local intensities $|\mathbf{E}_{loc}(\omega)|^2|\mathbf{E}_{loc}(\omega_R)|^2$ has a flatter behavior and no strong resonance is observed near the laser wavelength (green plots in Figure 6A).

To understand in which EF range our experimental values were, we estimated the possible EFs by using some common assumptions (SI, Section S7). The main problem is the estimation of the number of SERS active molecules. We adopted several common approximations with the maximal surface density of the monolayer Raman molecules to obtain an estimate for the EF of about 1.23×10^4 for 730–860 nm wavelengths (SI, Section S7). Given the surface and orientation averaging, this estimated EF is not unexpected for such a system.[44] What is more, the predicted SERS EFs are remarkably close to the experimental values (Figure 6B, red curve) within the 770–900 nm spectral range. However, for smaller and longer wavelengths the agreement between calculated and measured EFs becomes much worse up to an order of magnitude. For simulations, we used a constant. In summary, the predicted dependence of the averaged electromagnetic EF on the AuNP aspect ratio (PR wavelength) at a fixed 785 nm laser excitation is much flatter than initially expected once the orientation-averaging and Raman Stokes shift are determined. Nevertheless, it still exhibits larger variations than those observed experimentally, when the

https://dx.doi.org/10.1021/acs.jpcc.0c00991
J. Phys. Chem. C 2020, 124, 10647–10658

Table 1. Adsorption Parameters of NBT Molecules on AuNRs and SERS EFs

sample	nanorod concentration × 10^{10} part/mL	number of NBT molecules per one nanorod	NBT footprint nm^2	SERS EF
AuNR-890@NBT	7.33 ± 0.17	1.33×10^4	0.55	1.5×10^4
AuNR-788@NBT	7.04 ± 0.66	1.08×10^4	0.55	2.8×10^4
AuNR-700@NBT	6.45 ± 0.63	0.757×10^4	0.64	3.25×10^4

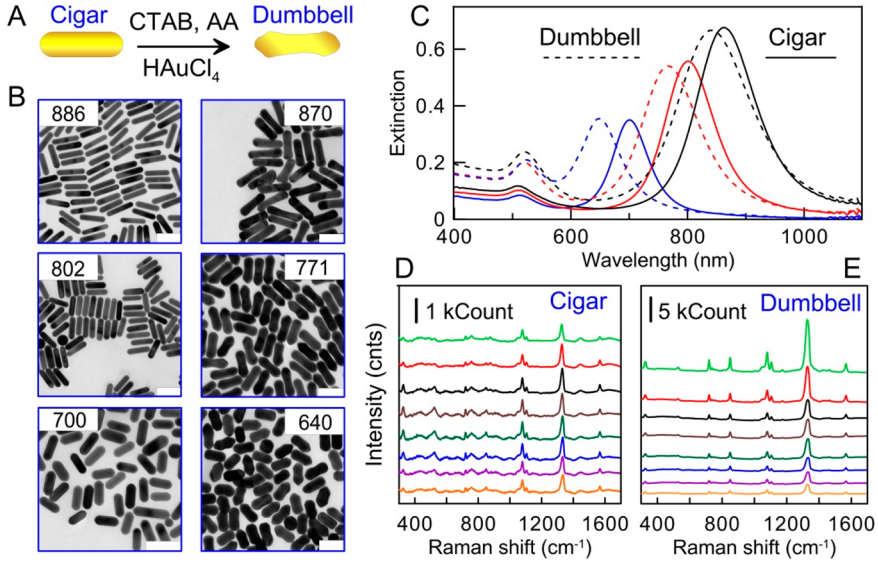

Figure 7. (A) Schematic transformation of cigar-shaped AuNRs into dumbbells. (B) TEM images of nanoparticles before and after AuNR/dumbbell reshaping. The main plasmonic peaks (in nm) are indicated on the images. The bars are 100 nm. (C) Spectral changes are illustrated with three AuNR/dumbbell pairs shown in panel B. SERS spectra of NBT adsorbed on the initial cigar-shaped AuNRs (D) and on dumbbells obtained after overgrowing the same AuNRs (E).

excitation wavelength is below the PR wavelength. Although the exact physical reasons behind this disagreement are unclear at the present, we can offer some possible explanations. One is photobleaching or photodestruction of the Raman molecules, as molecules with the highest EFs may be destroyed during the integration time. However, we observed similar dependences of the SERS spectra on the AuNR PR with two different spectrometers and different laser intensities. Further, NBT is much more photostable than, for example, rhodamine 6G and similar dyes. Another explanation could be related to the increased number of Raman active molecules for shorter AuNRs. However, to explain the observed discrepancies one would assume that the number of Raman reporters is increased by more than 1 order of magnitude. Given quite similar AuNR morphology for all aspect ratios this assumption seems questionable.

Quantifying the Number of Gold Nanorods and Number of Adsorbed NBT Molecules. In previous discussion, we assumed that the nanorod concentration for all the samples within one batch of etched nanorods is constant for each SERS experiment, because the etching of nanoparticles decreases their length but keeps their numbers. Nevertheless, we decided to verify this assumption with alternative AAS (Section S8) and spectrophotometry (Section S9) methods.

The second key point is the direct estimation of the reporter molecule amount on the rods. In the above discussion, we assumed that the number of adsorbed molecules is proportional to the nanoparticle surface area. Although this may be roughly the case but for our study this statement needs to be proven (Section S10).

For quantifying the number of gold nanorods and the number of adsorbed NBT molecules, we prepared an independent Set 3 of three AuNR-700, AuNR-788, and AuNR-890 samples by using the same synthesis and functionalization protocols as for Set 1. Specifically, we fabricated the initial AuNR-916 sample first and then obtained three samples with PRs at 890, 788, and 700 nm through the etching protocol (Figure S6 and Table S3).

The AAS concentrations of gold in etched samples are summarized in Table S4. Both variants of AAS methods (see Experimental and Theoretical Methods) gave similar reasonable decreasing concentrations for AuNR-890, 788, and 700 samples. Table S4 shows roughly constant nanorod concentrations (7.0 ± 0.7) × 10^{10} mL^{-1} in three etched samples, which are in agreement with our assumption based on the chemistry of nanorod etching.

For independent evaluation of nanorod concentration in the etched samples, we used two variants of spectrophotometry. The first one is based on the measurement of the plasmonic extinction peak and T-matrix simulations with TEM-derived statistical parameters of nanorods. As this approach is sensitive to such model parameters as the aspect ratio distribution and the optical constants of nanorods, we also used another variant based on the measurement of nanorod absorption at 450 nm. For wavelengths below 450 nm, the absorption of gold colloids is determined by the absorption of d-electrons in gold particles and is roughly proportional to the volume of particles irrespective to their shape and structure.[32,33] A detailed discussion of all technical points is given in Section S9, and the final data are summarized in Table S5. In excellent agreement with AAS data, Table S5 also shows roughly

https://dx.doi.org/10.1021/acs.jpcc.0c00991
J. Phys. Chem. C 2020, 124, 10647−10658

constant nanorods concentrations $(6.9 \pm 0.6) \times 10^{10}$ mL^{-1} in three etched samples. Thus, we have confirmed the constancy of nanorod concentration in the etched samples by two independent methods.

In Section S10, we provide a detailed description of quantifying the number of NBT molecules adsorbed on gold nanorods. Additional SERS measurements and calculations of SERS EFs with quantitative evaluation of NBT reporters per one nanorod are given in Section S10. Table 1 provides a summary of the main results.

Several conclusions can be drawn from the data of Table 1. First, the number of particles in etched samples is constant within ±8%. Second, the NBT adsorption footprint of 0.55 nm^2 is constant within ±10% and it is close to the topological polar surface area of NBT of 0.468 nm^2 (see ref 50). This means that the number of adsorbed NBT molecules per one nanorod is close to that for a monolayer packing density. In particular, for AuNR-890 the experimental number of adsorbed molecules per one nanorod $N_{NBT}^{1} = 1.33 \times 10^4$ is slightly less than the monolayer packing value $N_{NBT}^{1} = 7.32 \times 10^3/0.468 = 1.56 \times 10^4$. Third, the obtained SERS EFs are in agreement with previous estimations. Namely, for wavelengths shorter than the PR wavelength, the measured variations in SERS EFs are quite moderate in contrast to EM predictions.

Improvement of the SERS Response by Reshaping. It is well-known that gold nanorods can have different shapes (e.g., cigars, dog bones, or dumbbells). A small variation in shape can affect the SERS response significantly. Here, we demonstrate that a small shape variation indeed results in a greater effect on the SERS response than the particle PR tuning to the excitation laser wavelength. To this end, eight samples of cigar-shaped AuNR-900 were overgrown into dumbbells by the simple addition of an equal amount of $HAuCl_4$ and ascorbic acid (AA) to each AuNR sample. Note that the initial concentrations of Au in AuNR colloids with different PRs were different; thus, the transformation to dumbbells was higher for samples with a lower PR. The SERS responses of the initial AuNRs and final dumbbells were measured in solution (Figure 7).

From an optical point of view, the transformation of cigars into dumbbells (Figure 7B) leads to a blue shift of the longitudinal plasmonic peak and to a weak red shift of the transversal one (Figure 7C). For example, AuNRs-886 resulted in dumbbells with a plasmonic peak at 870 nm. This is due to a decrease in the particles' axial ratio, which was caused by a predominant increase in thickness. The reshaping effects are more pronounced for the shorter initial nanorods, as in this case the molar ratio of added to initial gold is higher. TEM images (Figure 7B) show the dumbbell morphology of the overgrown samples regardless of the original AuNR samples. More importantly, the SERS response of the dumbbells is about 5 times higher than that for the initial nanorods (Figure 7D,E). Note that this increase is larger than all the SERS peak variations that we observed when the PR of the nanorods was detuned within ±100 nm of the excitation wavelength. Because of the more pronounced shape transformation of short AuNRs into dumbbells, the SERS signal for short dumbbells is higher than that for long ones. Consequently, the tuning of the nanoparticle PR to the laser wavelength plays a much less important role for the maximization of the SERS response than does the transformation of the particles' shape from cigarlike rods to dumbbells.

CONCLUSION

It has been commonly accepted that the electromagnetic theory of SERS gives a reasonable estimate for the expected range of EFs despite the rather widespread reported experimental EFs. Although the actual measured EFs are strongly affected by many factors (e.g., the number of adsorbed Raman molecules or their distribution over the substrate's hot spots), there is a general consensus about the usability of the power law $I_{SERS} \sim |E_{loc}|^4$ for making a reasonable estimate of the SERS EFs. As a result, when simulating the SERS response for plasmonic nanostructures with a variable PR around the laser excitation wavelength, one arrives at extremely strong EF variations (within one or 2 orders of magnitude), even for moderate detuning (within ±100 nm).

We have experimentally reexamined the above theoretical predictions by using a simple, reproducible, and controllable model of AuNRs with a variable aspect ratio. By contrast with the previously reported ensemble measurements, we have used the etching method to fabricate a set of samples with a constant width and concentration, while the nanorod length was finely shortened. Because all samples were prepared from the same original batch of nanorods, there were no problems with variations in particle morphology, impurities, and concentrations that would be typical of the previously used independent synthesis. With two independent methods we have confirmed the constancy of nanorod concentration ($\sim 7 \times 10^{10}$ mL^{-1}) in etched samples. The number of adsorbed NBT molecules per one nanorod ($\sim 10^4$) has been determined by desorption of NBT molecules with DTT. For three etched samples (Set 3), we have found almost constant effective footprint ~0.55 nm^2 of NBT molecules adsorbed on AuNRs. This remarkable result means that the topology of NBT adsorption is close to the monolayer packing density with the topological polar surface area of NBT 0.468 nm^2.

With three independent sets of etched AuNRs and two measurement schemes (solution in a cuvette with waveguide spectrometers and sample drop on slides with a Raman microscope), we have come to similar conclusions. Namely, the experimental variations in the main SERS intensity of the adsorbed NBT molecules are quite moderate for nanorods with PRs varied around the laser wavelength of 785 nm within a wide range (650−925 nm). This finding is the first main result of our study. In order to account for this observation, we showed that SERS EF predictions must include orientation averaging and the effect of the Raman shift (beyond the common E^4-approximation). For PR wavelengths between 800 and 900 nm, both simulated and experimental EFs then show very small variations and are in remarkable agreement. However, for PR wavelengths between 650 and 800 nm, EM simulations still predict strong variations in the SERS intensity within 1 order of magnitude, which is in stark contrast to the experimental EFs. The exact reasons for such disagreement between measurements and EM simulations are unclear, and further work is needed to clarify the point.

In agreement with earlier results, we have also demonstrated that the reshaping of nanoparticles is a more important factor toward the highest SERS response than is the tuning of the plasmonic peak for on-resonance excitation. Specifically, the overgrowth of cigarlike nanorods to a dumbbell morphology increased the SERS response 5-fold. Thus, the rational design of shape morphology is more important for SERS optimization than the exact tuning of the PR to the excitation wavelength. In

https://dx.doi.org/10.1021/acs.jpcc.0c00991
J. Phys. Chem. C 2020, 124, 10647−10658

practice, detuning within ±100 nm may be quite acceptable. This is the second main finding of our study.

Finally, we have examined the Bg contribution to the measured SERS spectra from AuNR solutions, in analogy with the earlier data for single-particle measurements.[21] In our case, the experimental range of the aspect ratio and PR variations were wider than those reported previously,[21,29] but the main features in the spectral behavior of the Bg were similar. This means that the previously suggested procedure for the Bg correction of SERS spectra could be applicable not only to single-particle spectra[21] but also to ensemble measuring. The dependence of the Bg spectra on the particle aspect ratio is consistent with both the PL from an AuNR ensemble and the elastic light scattering of a very weak laser Bg by the same AuNR ensemble. This is the third main result of our study. However, further work is needed to explore this issue in detail.

We hope that the described reexamination study and the observed discrepancy between measured and predicted dependencies of the SERS intensity on the AuNR aspect ratio will stimulate further research on the plasmonically enhanced SERS of colloidal and single particles of various morphologies.

■ ASSOCIATED CONTENT

Supporting Information

The Supporting Information is available free of charge at https://pubs.acs.org/doi/10.1021/acs.jpcc.0c00991.

Section S1: Characterization of as-prepared AuNR-900 and samples after etching, including Figure S1 and Table S1. Section S2: T-matrix simulation of extinction spectra for AuNR colloids. Section S3: TEM and UV−vis characterization of the AuNR-925 sample and SERS measurements with Ocean Optics Raman spectrometer and Renishaw inVia Raman microscope (Figure S2 and Table S2). Section S4: SERS spectra of NBT adsorbed on 30 nm Au spheres and on 140 × 20 nm AuNRs (Figure S3). Section S5: SERS spectra of 5-fold diluted samples (Figure S4). Section S6: FDTD simulations of the near-field distribution (Figure S5). Section 7: Estimation of the SERS enhancement factors. Section S8: Quantifying the gold concentration in etched samples by AAS. Section S9: Quantifying the gold concentration in etched samples by UV−vis spectrophotometry. Section S10: Quantifying the number of NBT molecules adsorbed on gold nanorods. Section S11: SERS spectra and enhancement factors for Set 3 of AuNRs (PDF)

■ AUTHOR INFORMATION

Corresponding Author

Nikolai G. Khlebtsov − *Institute of Biochemistry and Physiology of Plants and Microorganisms, Russian Academy of Sciences, Saratov 410049, Russia; Saratov National Research State University, Saratov 410012, Russia;* orcid.org/0000-0002-2055-7784; Email: khlebtsov@ibppm.ru

Authors

Boris N. Khlebtsov − *Institute of Biochemistry and Physiology of Plants and Microorganisms, Russian Academy of Sciences, Saratov 410049, Russia;* orcid.org/0000-0003-3996-5750

Vitaly A. Khanadeev − *Institute of Biochemistry and Physiology of Plants and Microorganisms, Russian Academy of Sciences, Saratov 410049, Russia*

Andrey M. Burov − *Institute of Biochemistry and Physiology of Plants and Microorganisms, Russian Academy of Sciences, Saratov 410049, Russia*

Eric C. Le Ru − *The MacDiarmid Institute for Advanced Materials and Nanotechnology, School of Chemical and Physical Sciences, Victoria University of Wellington, Wellington 6140, New Zealand;* orcid.org/0000-0002-3052-9947

Complete contact information is available at: https://pubs.acs.org/10.1021/acs.jpcc.0c00991

Notes

The authors declare no competing financial interest.

■ ACKNOWLEDGMENTS

This research was supported by the Russian Scientific Foundation (Project No. 18-14-00016). The work on quantifying the gold nanorod and NBT concentrations was supported by grants from the Russian Foundation of Basic Research (BNK, Project No. 18-52-7803) and from the President of Russian Federation (VAK, Project No. MK-1867.2019.2). The work by VAK on AuNR synthesis was supported by the Russian Scientific Foundation (Project No. 19-72-00120). We thank D. N. Tychinin (IBPPM RAS) for his help in the preparation of the manuscript and Dr. P. N. Melentiev (ISAN, Troitsk, Moscow) for discussion of SERS background.

■ REFERENCES

(1) Wang, Y.; Yan, B.; Chen, L. SERS Tags: Novel Optical Nanoprobes for Bioanalysis. *Chem. Rev.* **2013**, *113*, 1391−1428.

(2) Fabris, L. Gold-Based SERS Tags for Biomedical Imaging. *J. Opt.* **2015**, *17*, 114002.

(3) Mohs, A. M.; Mancini, M. C.; Singhal, S.; Provenzale, J. M.; Leyland-Jones, B.; Wang, M. D.; Nie, S. Hand-held Spectroscopic Device for in Vivo and Intraoperative Tumor Detection: Contrast Enhancement, Detection Sensitivity, and Tissue Penetration. *Anal. Chem.* **2010**, *82*, 9058−9065.

(4) Wang, Y.; Kang, S.; Khan, A.; Ruttner, G.; Leigh, S. Y.; Murray, M.; Abeytunge, S.; Peterson, G.; Rajadhyaksha, M.; Dintzis, S.; Javid, S.; Liu, J. T.C.; et al.et al Quantitative Molecular Phenotyping with Topically Applied SERS Nanoparticles for Intraoperative Guidance of Breast Cancer Lumpectomy. *Sci. Rep.* **2016**, *6*, 21242.

(5) Karabeber, H.; Huang, R.; Iacono, P.; Samii, J. M.; Pitter, K.; Holland, E. C.; Kircher, M. F. Guiding Brain Tumor Resection Using Surface-Enhanced Raman Scattering Nanoparticles and a Hand-Held Raman Scanner. *ACS Nano* **2014**, *8*, 9755−9766.

(6) Lim, D. K.; Jeon, K. S.; Hwang, J. H.; Kim, H.; Kwon, S.; Suh, Y. D.; Nam, J. M. Highly Uniform and Reproducible Surface-Enhanced Raman Scattering from DNA-Tailorable Nanoparticles with 1-nm Interior Gap. *Nat. Nanotechnol.* **2011**, *6*, 452−460.

(7) Gandra, N.; Singamaneni, S. Bilayered Raman-Intense Gold Nanostructures with Hidden Tags (BRIGHTs) for High-Resolution Bioimaging. *Adv. Mater.* **2013**, *25*, 1022−1027.

(8) Le Ru, E. C.; Meyer, M.; Blackie, E.; Etchegoin, P. G. Advanced Aspects of Electromagnetic SERS Enhancement Factors at a Hot Spot. *J. Raman Spectrosc.* **2008**, *39*, 1127−1134.

(9) Haynes, C. L.; Van Duyne, R. P. Plasmon-Sampled Surface-Enhanced Raman Excitation Spectroscopy. *J. Phys. Chem. B* **2003**, *107*, 7426−7433.

(10) McFarland, A. D.; Young, M. A.; Dieringer, J. A.; Van Duyne, R. P. Wavelength-Scanned Surface-Enhanced Raman Excitation Spectroscopy. *J. Phys. Chem. B* **2005**, *109*, 11279−11285.

(11) Zhao, J.; Dieringer, J. A.; Zhang, X.; Schatz, G. C.; Van Duyne, R. P. Wavelength-Scanned Surface-Enhanced Resonance Raman Excitation Spectroscopy. *J. Phys. Chem. C* **2008**, *112*, 19302−19310.
(12) El-Sayed, M. A. Some Interesting Properties of Metals Confined in Time and Nanometer Space of Different Shapes. *Acc. Chem. Res.* **2001**, *34*, 257−264.
(13) Boca, S. C.; Astilean, S. Detoxification of Gold Nanorods by Conjugation with Thiolated Poly(ethylene glycol) and Their Assessment as SERS-active Carriers of Raman Tags. *Nanotechnology* **2010**, *21*, 235601.
(14) McLintock, A.; Cunha-Matos, C. A.; Zagnoni, M.; Millington, O. R.; Wark, A. W. Universal Surface-Enhanced Raman Tags: Individual Nanorods for Measurements from the Visible to the Infrared (514−1064 nm). *ACS Nano* **2014**, *8*, 8600−8609.
(15) Orendorff, C. J.; Gearheart, L.; Janaz, N. R.; Murphy, C. J. Aspect Ratio Dependence on Surface Enhanced Raman Scattering Using Silver and Gold Nanorod Substrates. *Phys. Chem. Chem. Phys.* **2006**, *8*, 165−170.
(16) Smitha, S. L.; Gopchandran, K. G.; Ravindran, T. R.; Prasad, V. S. Gold Nanorods with Finely Tunable Longitudinal Surface Plasmon Resonance as SERS Substrates. *Nanotechnology* **2011**, *22*, 265705.
(17) Sivapalan, S. T.; DeVetter, B. M.; Yang, T. K.; van Dijk, T.; Schulmerich, M. V.; Carney, P. S.; Bhargava, R.; Murphy, C. J. Off-Resonance Surface-Enhanced Raman Spectroscopy from Gold Nanorod Suspensions as a Function of Aspect Ratio: Not What We Thought. *ACS Nano* **2013**, *7*, 2099−2105.
(18) Lin, K.-Q.; Yi, J.; Hu, S.; Liu, B. J.; Liu, J. Y.; Wang, X.; Ren, B. Size Effect on SERS of Gold Nanorods Demonstrated via Single Nanoparticle Spectroscopy. *J. Phys. Chem. C* **2016**, *120*, 20806−20813.
(19) Saute, B.; Premasiri, R.; Zieglera, L.; Narayanan, R. Gold Nanorods as Surface Enhanced Raman Spectroscopy Substrates for Sensitive and Selective Detection of Ultra-low Levels of Dithiocarbamate Pesticides. *Analyst* **2012**, *137*, 5082.
(20) Doherty, M. D.; Murphy, A.; McPhillips, J.; Pollard, R. J.; Dawson, P. Wavelength Dependence of Raman Enhancement from Gold Nanorod Arrays: Quantitative Experiment and Modeling of a Hot Spot Dominated System. *J. Phys. Chem. C* **2010**, *114*, 19913−19919.
(21) Lin, K.-Q.; Yi, J.; Zhong, J.-H.; Hu, S.; Liu, B.-J.; Liu, J.-Y.; Zong, C.; Lei, Z.-C.; Wang, X.; Aizpurua, J.; et al.et al Plasmonic Photoluminescence for Recovering Native Chemical Information from Surface-enhanced Raman Scattering. *Nat. Commun.* **2017**, *8*, 14891−14897.
(22) Félidj, N.; Aubard, J.; Lévia, G.; Krenn, J. R.; Hohenau, A.; Schider, G.; Leitner, A.; Aussenegg, F. R. Optimized Surface-Enhanced Raman Scattering on Gold Nanoparticle Arrays. *Appl. Phys. Lett.* **2003**, *82*, 3095−3097.
(23) Schatz, G. C.; Young, M. A.; Van Duyne, R. P. Electromagnetic Mechanism of SERS. In *Surface-Enhanced Raman Scattering−Physics and Applications*; Kneipp, K., Moskovits, M., Kneipp, H., Eds.; Springer: Berlin, 2006; Vol. *103*, pp 19−46.
(24) Le Ru, E. C.; Etchegoin, P. G. *Principles of Surface Enhanced Raman Spectroscopy and Related Plasmonic Effects*; Elsevier: Amsterdam, 2009.
(25) Rodrıguez-Fernandez, J.; Perez-Juste, G.; Mulvaney, P.; Liz-Marzan, L. M. Spatially-Directed Oxidation of Gold Nanoparticles by Au(III)-CTAB Complexes. *J. Phys. Chem. B* **2005**, *109*, 14257−14261.
(26) Khlebtsov, B. N.; Khanadeev, V. A.; Burov, A. M.; Khlebtsov, N. G. Tuning of Plasmon Resonance of Gold Nanorods by Controlled Etching. *Colloid J.* **2015**, *77*, 652−660.
(27) Raziman, T. V.; Somerville, W. R. C.; Martin, O. J. F.; Le Ru, E. C. Accuracy of Surface Integral Equation Matrix Elements in Plasmonic Calculations. *J. Opt. Soc. Am. B* **2015**, *32*, 485−492.
(28) Somerville, W. R. C.; Auguié, B.; Le Ru, E. C. SMARTIES: User-Friendly Codes for Fast and Accurate Calculations of Light Scattering by Spheroids. *J. Quant. Spectrosc. Radiat. Transfer* **2016**, *174*, 39−55.
(29) Fang, Y.; Chang, W.-S.; Willingham, B.; Swanglap, P.; Dominguez-Medina, S.; Link, S. Plasmon Emission Quantum Yield of Single Gold Nanorods as a Function of Aspect Ratio. *ACS Nano* **2012**, *6*, 7177−7184.
(30) Cai, Y.-Y.; Liu, J. G.; Tauzin, L. J.; Huang, D.; Sung, E.; Zhang, H.; Joplin, A.; Chang, W.-S.; Nordlander, P.; Link, S. Photoluminescence of Gold Nanorods: Purcell Effect Enhanced Emission from Hot Carriers. *ACS Nano* **2018**, *12*, 976−985.
(31) Khlebtsov, B. N.; Khanadeev, V. A.; Ye, J.; Sukhorukov, G. B.; Khlebtsov, N. G. Overgrowth of Gold Nanorods by Using a Binary Surfactant Mixture. *Langmuir* **2014**, *30*, 1696−1703.
(32) Haiss, W.; Thanh, N. T. K.; Aveard, J.; Fernig, D. G. Determination of Size and Concentration of Gold Nanoparticles from UV-Vis Spectra. *Anal. Chem.* **2007**, *79*, 4215−4221.
(33) Khlebtsov, N. G. Determination of Size and Concentration of Gold Nanoparticles from Extinction Spectra. *Anal. Chem.* **2008**, *80*, 6620−6625.
(34) Johnson, P. B.; Christy, R. W. Optical Constants of the Noble Metals. *Phys. Rev. B* **1972**, *6*, 4370−4379.
(35) Khlebtsov, B.; Khanadeev, V.; Pylaev, T.; Khlebtsov, N. A New T-Matrix Solvable Model for Nanorods: TEM-Based Ensemble Simulations Supported by Experiments. *J. Phys. Chem. C* **2011**, *115*, 6317−6323.
(36) Kern, A. M.; Martin, O. J. F. Surface Integral Formulation for 3D Simulations of Plasmonic and High Permittivity Nanostructures. *J. Opt. Soc. Am. A* **2009**, *26*, 732.
(37) Khlebtsov, B. N.; Khanadeev, V. A.; Khlebtsov, N. G. Observation of Extra-High Depolarized Light Scattering Spectra from Gold Nanorods. *J. Phys. Chem. C* **2008**, *112*, 12760−12768.
(38) Link, S.; El-Sayed, M. A. Simulation of the Optical Absorption Spectra of Gold Nanorods as a Function of Their Aspect Ratio and the Effect of the Medium Dielectric Constant. *J. Phys. Chem. B* **2005**, *109*, 10531−10532.
(39) Rayleigh, L. On the Incidence of Aerial and Electric Waves upon Small Obstacles in the Form of Ellipsoids or Elliptic Cylinders, and on the Passage of Electric Waves through a Circular Aperture in a Conducting Screen. *Philos. Magazine* **1897**, *44* (266), 28−52.
(40) Gans, R. Über die Form ultramikroskopischer Goldteilchen. *Ann. Phys.* **1912**, *342* (5), 881−900.
(41) Prescott, W.; Mulvaney, P. J. Gold Nanorod Extinction Spectra. *J. Appl. Phys.* **2006**, *99*, 123504.
(42) Khlebtsov, B. N.; Bratashov, D. N.; Khlebtsov, N. G. Tip-Functionalized Au@Ag Nanorods as Ultrabright Surface-Enhanced Raman Scattering Probes for Bioimaging in Off-Resonance Mode. *J. Phys. Chem. C* **2018**, *122*, 17983−17993.
(43) Fang, Y.; Seong, N. H.; Dlott, D. D. Measurement of the Distribution of Site Enhancements in Surface-Enhanced Raman Scattering. *Science* **2008**, *321*, 388−392.
(44) Le Ru, E. C.; Blackie, E.; Meyer, M.; Etchegoin, P. G. Surface Enhanced Raman Scattering Enhancement Factors: A Comprehensive Study. *J. Phys. Chem. C* **2007**, *111*, 13794−13803.
(45) Teguh, J. S.; Liu, F.; Xing, B.; Yeow, E. K. L. Surface-Enhanced Raman Scattering (SERS) of Nitrothiophenol Isomers Chemisorbed on TiO2. *Chem. - Asian J.* **2012**, *7*, 975−981.
(46) Khlebsov, B. N.; Bratashov, D. N.; Byzova, N. A.; Dzantiev, B. B.; Khlebtsov, N. G. SERS-Based Lateral Flow Immunoassay of Troponin I Using Gap-Enhanced Raman Tags. *Nano Res.* **2019**, *12*, 413−420.
(47) Lakowicz, J. R. *Principles of Fluorescence Spectroscopy*, 3rd ed.; Springer: Berlin, 2006.
(48) Cai, Y.-Y.; Sung, E.; Zhang, R.; Lawrence, R. T.; Liu, J. G.; Ostovar, B.; Zhang, Y.; Chang, W.-S.; Nordlander, P.; Link, S. Anti-Stokes Emission from Hot Carriers in Gold Nanorods. *Nano Lett.* **2019**, *19*, 1067−1073.
(49) Khlebtsov, N. G.; Trachuk, L. A.; Melnikov, A. G. Plasmon Resonances of Silver and Gold Nanorods. *Proc. SPIE* **2012**, *5475*, 1−11.
(50) URL: https://pubchem.ncbi.nlm.nih.gov/compound/4-Nitrothiophenol. Accessed 17 April 2020.

https://dx.doi.org/10.1021/acs.jpcc.0c00991
J. Phys. Chem. C 2020, 124, 10647−10658

Supporting Information

Reexamination of Surface-Enhanced Raman Scattering from Gold Nanorods as a Function of Aspect Ratio and Shape

Boris N. Khlebtsov,[1,*] *Vitaly A. Khanadeev,*[1] *Andrey M. Burov,*[1] *Eric C. Le Ru*[3], *and Nikolai G. Khlebtsov*[1,2,*]

[1]Institute of Biochemistry and Physiology of Plants and Microorganisms, Russian Academy of Sciences, 13 Prospekt Entuziastov, Saratov 410049, Russia

[2]Saratov National Research State University, 83 Ulitsa Astrakhanskaya, Saratov 410012, Russia

[3]The MacDiarmid Institute for Advanced Materials and Nanotechnology, School of Chemical and Physical Sciences, Victoria University of Wellington, P.O. Box 600, Wellington 6140, New Zealand

Section S1. Characterization of as-prepared AuNR-907 and samples after etching

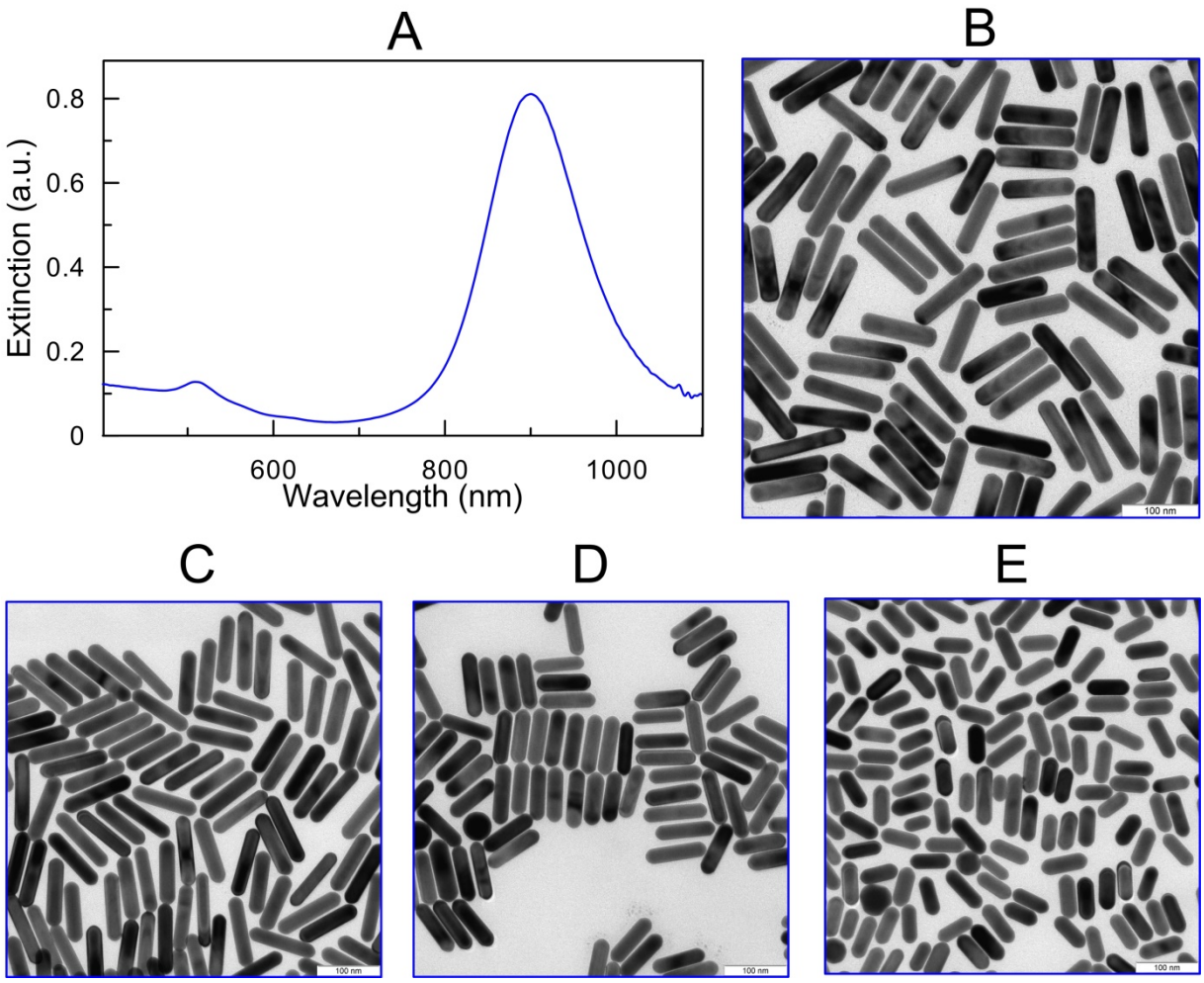

Figure S1. Extinction spectrum (A) and TEM images of the initial (B) and etched AuNRs after addition of 25 (C), 100 (D), and 175 (E) μL of $HAuCl_4$ to 10 mL of the initial nanorods.

Table S1. PR wavelength, length, width and aspect ratio of the initial and etched AuNRs (Set 1)

Sample	Amount of added* 10 mM $HAuCl_4$, μL	PR wavelength nm	Length nm	Width nm	Aspect ratio, AR
AuNR-900	0	900	109.5±5.8	25.5±1.2	4.30±0.34
AuNR-890	25	886	106.0±5.1	25.8±1.2	4.28±0.30
AuNR-860	50	863	101.7±5.1	25.8±1.4	3.95±0.31
AuNR-840	75	840	98.7±5.3	26.6±1.3	3.63±0.28
AuNR-800	100	802	96.2±5.1	25.5±1.6	3.50±0.24
AuNR-790	112.5	788	93.3±5.5	26.8±1.4	3.28±0.23
AuNR-750	125	751	90.1±5.2	26.8±1.5	3.04±0.25
AuNR-730	150	727	82.2±5.4	26.4±1.2	2.82±0.21
AuNR-700	175	700	68.0±5.0	26.8±1.2	2.64±0.18

*To 10 mL of initial AuNRs

For cigars with total length L and diameter d the surface area equals $S = \pi dL$. For the initial rods this gives $S_{900} = S_0 = 8.8\times10^3\,\mathrm{nm}^2$. For other nanorods, the ratio of the surface area is given by $S_{PR} / S_0 = dL / d_0 L_0$. This ratio was used for normalization of measured SERS peaks in Figure 2B.

Section S2. T-matrix simulation of extinction spectra for AuNR colloids.

The orientation-averaged extinction, scattering, and absorption cross sections of a single particle are given by the following T-matrix analytical solutions:[1]

$$\langle C_{ext}\rangle = \pi a_0^2 Q_{ext} = \frac{2\pi}{k^2}\mathrm{Re}\sum_{n=1,m=-n,i=1}^{\infty,n,2} T^{ii}_{mn,mn}\,, \tag{S1}$$

$$\langle C_{sca}\rangle = \pi a_0^2 Q_{sca} = \frac{2\pi}{k^2}\sum_{nn',mm',ij}^{\infty,n,2}\left|T^{ij}_{mn,m'n'}\right|^2,\ \langle C_{abs}\rangle = \langle C_{ext}\rangle - \langle C_{sca}\rangle\,. \tag{S2}$$

where $a_0 = \left(3V/4\pi\right)^{1/3}$ is the equivolume radius. The T-matrix elements are defined by six indexes (m,n,m',n',i,j), corresponding to the (m,n) indexes of spherical harmonics and $i,j = 1,2$ indexes of the $T^{i,j}$ submatrices. To calculate the extinction of a polydisperse AuNR

colloid, we consider a two-ensemble model consisting of a distribution of n_R types of rods and a distribution of n_S types of byproduct particles, whose shape is close to spherical (see TEM images):

$$n_{Ri} = N_{Ri} / \sum_{i=1}^{n_R} N_{Ri} , \quad n_{Si} = N_{Si} / \sum_{i=1}^{n_S} N_{Si} , \tag{S3}$$

where N_{Ri} and N_{Si} are the concentrations (number of particles per unit volume, e.g., 1 mL) of the i*th* type of rods and impurities, respectively, $N = N_R + N_S = \sum_{i=1}^{n_R} N_{Ri} + \sum_{i=1}^{n_S} N_{Si}$ is the total concentration. Then the extinction of this polydisperse ensemble is given by the following relationship:[2]

$$A_{ext} = \frac{Nl}{\ln 10}\left[w_R \sum_{i=1}^{n_R} n_{Ri} \langle C_{ext,Ri} \rangle + w_S \sum_{i=1}^{n_S} n_{Si} \langle C_{ext,Si} \rangle \right]. \tag{S4}$$

where $w_S = N_S / N$ and $w_R = N_R / N = 1 - w_S$. The average total volume of particles (dispersed in 1 mL of suspension) equals

$$V_t = \frac{4\pi}{3}\left[w_R \sum_{i=1}^{n_R} n_{Ri} a_{0Ri}^3 + w_S \sum_{j=1}^{n_S} n_{Si} a_{0Sj}^3 \right] = \frac{4\pi}{3} a_{\text{ev}}^3 , \tag{S5}$$

where $a_{0Ri} = \left(3V_{Ri} / 4\pi\right)^{1/3}$ and $a_{0Si} = \left(3V_{Si} / 4\pi\right)^{1/3}$ are equivolume radii of particles from each distribution. In Eq. (S5) a_{ev} is the average-volume radius of the whole ensemble. The total concentration of particles equals

$$N = c_g / [\rho_g V_t] , \tag{S6}$$

where c_g is the mass-per-unit-volume concentration of gold and ρ_g is the gold density. Eq. (S4) can be rewritten as

$$A_{ext} = \frac{Nl}{\ln 10} \langle C_{ext} \rangle . \tag{S7}$$

Here we have introduced the orientation averaged extinction cross section of the polydisperse ensemble given by the following relation:

$$\langle C_{ext}\rangle = w_R \sum_{i=1}^{n_R} n_{Ri}\langle C_{ext,Ri}\rangle + w_S \sum_{i=1}^{n_S} n_{Si}\langle C_{ext,Si}\rangle$$
$$= w_R \sum_{i=1}^{n_R} n_{Ri}\pi a_{0Ri}^2\langle Q_{ext,Ri}\rangle + w_S \sum_{i=1}^{n_S} n_{Si}\pi a_{0Si}^2\langle Q_{ext,Si}\rangle\,, \tag{S8}$$

where the extinction efficiencies of each type of particle are normalized to the corresponding geometrical cross sections $\pi a_{0R(S)i}^2$.

From an experimental point of view, it is convenient to express the measured extinction as a function of the mass-per-unit-volume concentration rather than in terms of the particle concentration. Taking into account Eqs. (S6) and (S7), we recast Eq. (S4) as

$$A_{ext} = \frac{c_g l}{\ln 10 \rho_g V_t}\langle C_{ext}\rangle\,. \tag{S9}$$

Eq. (S9) is convenient if the mass volume concentration is known and does not change during experimental manipulations. However, in our etching experiments, the particle number concentration rather than the mass-per-unit-volume concentration was constant. Therefore, according to Eq. (S7), the changes in the measured extinction of the etched samples scale like changes in the average extinction cross-section. By combining Eqs (S6), (S7) and (S9) we can express the average extinction cross section $\langle C_{ext}\rangle$ as

$$\langle C_{ext}\rangle = 0.321 a_{\mathrm{ev}}^3 A_{ext}, (\mathrm{nm}^2)\,, \tag{S10}$$

where our experimental parameters $l = 1$ cm and $c_g = 58\times10^{-6}$ g/mL have been taken into account. In Eq. (S10) the average-volume radius a_{ev} is expressed in nm.

Another convenient expression for normalization of the etched samples extinction can be obtained by using Eq. (S7) at the PR wavelength of the initial sample to find the number concentration, N, which is then the same in all etched samples

$$N = \frac{\ln 10}{\langle C_{ext}^0(\lambda_{\max})\rangle l} A_{ext}^0(\lambda_{\max})\,. \tag{S11}$$

After substituting Eq. (S11) into Eq. (S7), we get

$$A_{ext}(\lambda) = \langle C_{ext}(\lambda) \rangle \frac{A^0_{ext}(\lambda_{\max})}{\langle C^0_{ext}(\lambda_{\max}) \rangle}. \quad \text{(S12)}$$

This equation was used to normalize the T-matrix plots in Fig. 1G of the main text.

To simulate the ensemble aspect ratio polydispersity we used the normal distribution

$$f(x = AR / AR_{av}) = const \times \exp\left[-(x-1)^2 / 2\sigma^2_{AR} \right], \quad \text{(S13)}$$

where $\sigma_{AR} = \Delta AR / AR_{av}$ is the normalized standard deviation. From TEM images, the values of σ_{AR} are rather small and vary between 0.05 (final etched AuNRs) and 0.08 (the initial AuNRs). For simplicity, we simulated the extinction spectra with a constant value of $\sigma_{AR} = 0.06$, which results in a slightly broadened simulated spectra compared to the experimental ones for small AuNRs. Further, the proportion of byproduct particles was small and we therefore set $w_S = N_S / N = 0$ in all calculation. Addition of a small fraction (0.03) of byproducts to the whole ensemble resulted in more pronounced short wavelength peaks at 520 nm as compared to the experimental ones.

Section S3. TEM, UV-vis characterization of AuNR-925 sample and SERS measurements with Ocean Optics Raman spectrometer and Renishaw inVia Raman microscope

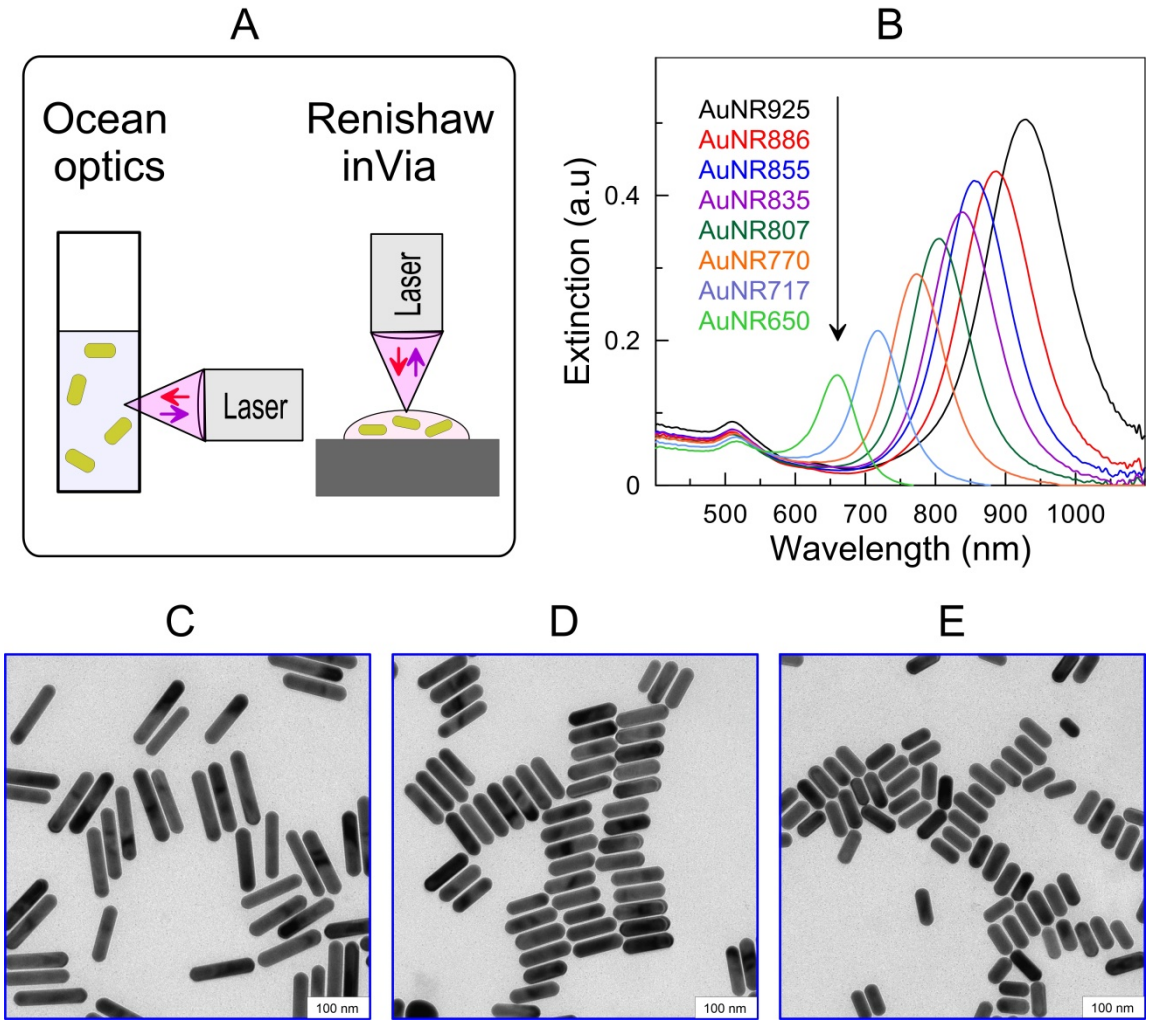

Figure S2. (A) Scheme of SERS measurements using the Ocean Optics peak seeker pro 785 and the Renishaw inVia 785 Raman microscope. (B) Extinction spectra of etched AuNR samples with PR wavelengths from 925 to 650 nm. TEM images of AuNR samples with aspect ratios $AR = 4.76 \pm 0.33$ (C), 3.44 ± 0.28 (D), 2.45 ± 0.22 (E) and PR wavelengths 925, 770, and 650 nm, respectively.

Table S2. PR wavelength, length, width and aspect ratio of the initial and etched AuNRs (Set 2)

Sample	Amount of added* 10 mM $HAuCl_4$, μL	PR wavelength, nm	Length, nm	Width, nm	Aspect ratio, AR
AuNR-925	0	925	117.9±6.6	25.4±1.5	4.76±0.33
AuNR-890	25	886	111.5±6.4	25.6±1.34	4.24±0.30
AuNR-850	50	854	101.7±5.1	26.3±1.4	3.88±0.29
AuNR-840	100	837	94.9±7.2	26.4±1.6	3.79±0.30
AuNR-790	112.5	788	94.9±7.2	26.3±1.4	3.54±0.26
AuNR-770	125	769	85.9±5.3	25.5±1.5	3.31±0.23
AuNR-710	150	714	74.9±6.6	26.2±1.8	2.80±0.22
AuNR-650	175	650	60.8±4.7	25.2±1.2	2.37±0.18

*To 10 mL of the initial AuNRs.

Section S4. SERS spectra of NBT adsorbed on 30 nm Au spheres and 140×20 nm AuNRs

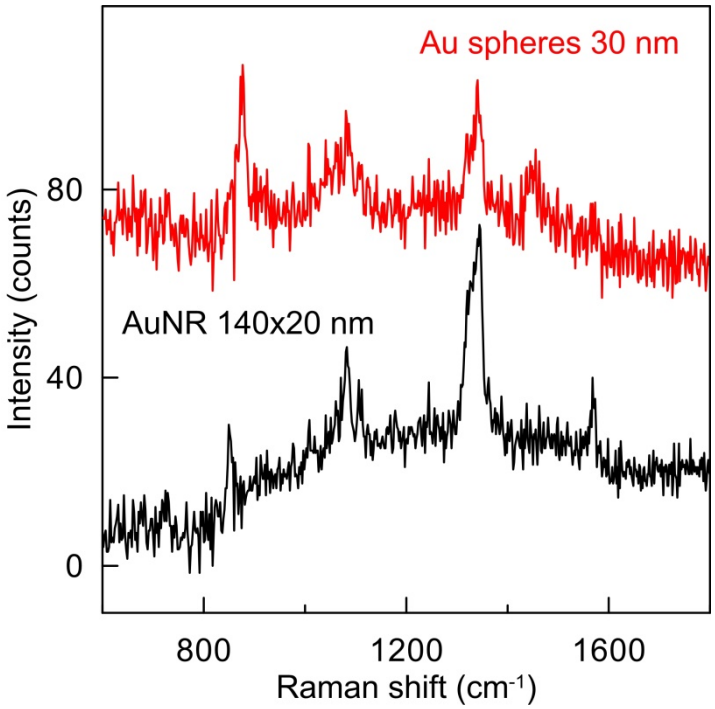

Figure S3. SERS spectra of NBT molecules adsorbed on 30 nm spherical Au nanoparticles and on long AuNRs (140×20 nm) with longitudinal PR wavelength of 1065 nm.

Section S5. SERS spectra of 5-fold diluted samples

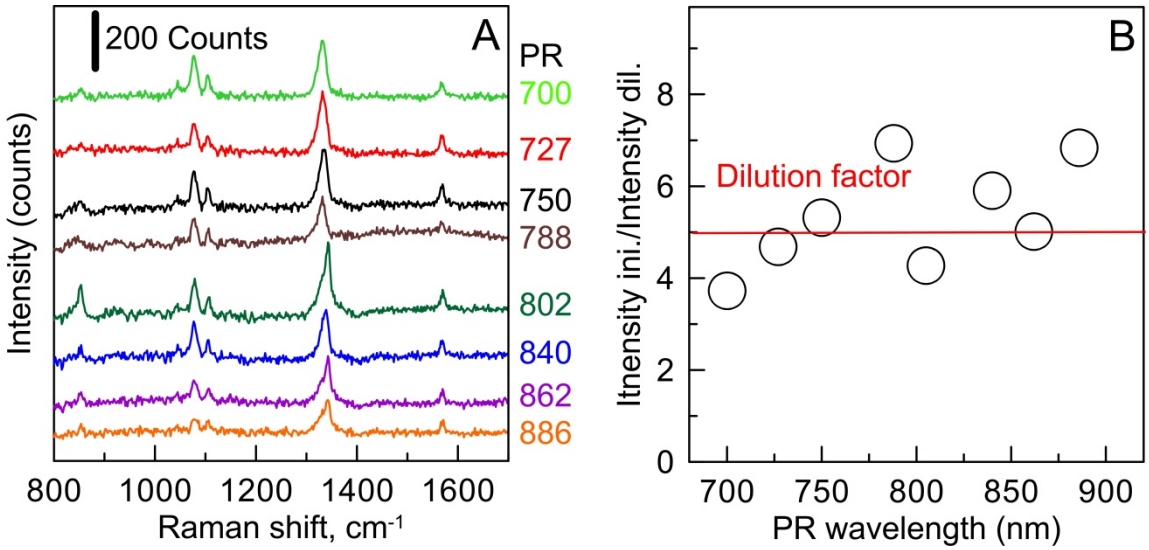

Figure S4. (A) SERS spectra of diluted (1:5) AuNR–NBT colloids with PRs from 700 to 886 nm. The background was subtracted by using a polynomial fit. (B) The ratio between peak intensities at 1342 cm^{-1} for the initial and diluted samples.

Section S6. FDTD simulations of the near field distribution

To reconstruct the local field distribution, we used a standard 2D map in the equatorial plane and a special $(x, y, z, \mathrm{Re}(\mathbf{E}))$ map by plotting the electric field vectors $\mathrm{Re}(\mathbf{E})$ for each (x, y, z) point on the particle surface. In such a representation, the field direction was determined by the Cartesian components of $\mathrm{Re}(\mathbf{E})$ and the field modulus $|\mathrm{Re}(\mathbf{E})|$ was mapped with color.

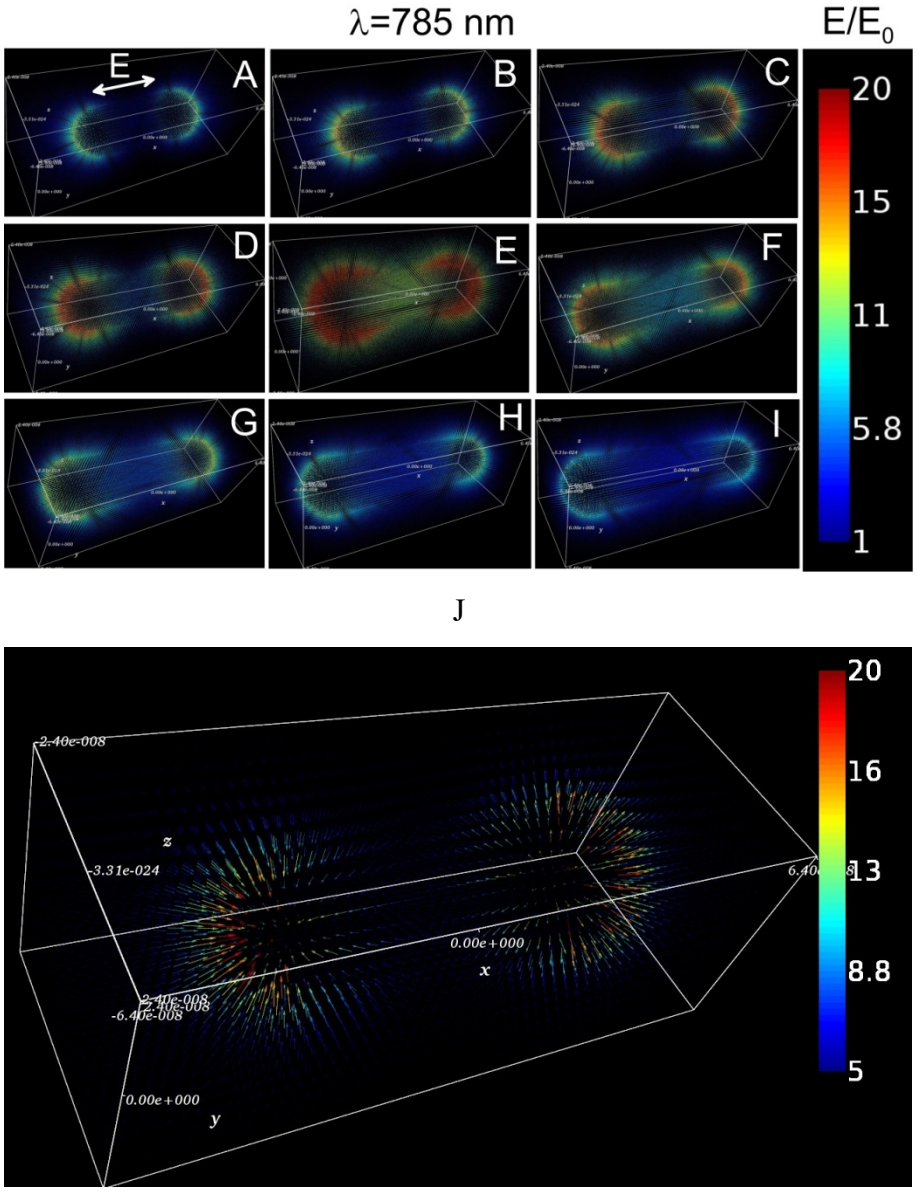

Figure S5. Simulated 3D field distributions where each point is an arrow, with a direction corresponding to the real part of calculated local field. The amplitude of that vector is given by a color map scale. Calculations for AuNRs with width of 26 nm and length of 74 (A), 78(B), 82 (C), 86 (D), 90 (E), 94 (F), 98 (G), 102 (H) and 106 nm (I). Panel (J) shows an enlarged image of a 3D distribution of the local field modulus on the surface of AuNR 82×26 nm.

Section S7. Estimation of the SERS enhancement factors

The fundamental EF is defined as the ratio of the SERS and normal Raman intensities normalized to the corresponding number of excited molecules

$$EF = \frac{I_{SERS} / N_{SERS}}{I_{Raman} / N_{Raman}}, \quad \text{(S14)}$$

where both SERS and Raman intensities should be measured under identical experimental conditions, including laser wavelength and power P, accumulation time, etc. The above definition of EF presents several problems, as it is difficult to estimate N_{SERS} for different substrates and to measure the normal Raman intensity from molecular reporters with the same laser power and accumulation time as those used for SERS measurements. Here, we adopt a simplest approximation based on the assumption of monolayer covering of Raman molecules according to their topological polar surface area 0.468 nm^2.[3] This gives an upper limit for the concentration of Raman reporters per one nanorod and, consequently, a lower limit on the EF. From TEM data, the average radius of equivolume sphere of the AuNRs is 23.4 nm. This gives an AuNR volume $V = 5.37 \times 10^4\,\mathrm{nm}^3$ and an average particle mass $m = \rho V = 19.32\mathrm{g/cm}^3 \times 5.37 \times 10^4\,\mathrm{nm}^3 = 1.04 \times 10^{-15}\,g$. T-matrix simulations for the mass-per-unit-volume concentration of AuNRs of $57\,\mathrm{mg/L}$ give an optical density in a 1-cm cuvette of about 5.3 at the PR wavelength. The measured optical density in the 1-cm cuvette at the PR wavelength is in fact 3.75, thus giving a mass-per-unit volume concentration of Au of $c = 41\mathrm{mg/L}$ and a particle concentration of $N = 3.9 \times 10^{10}\,\mathrm{part/mL}$.

For cigar-like model, the total AuNR surface is $S = \pi dL = 8.8 \times 10^3\,\mathrm{nm}^2$. By dividing this area by the NBT molecule footprint we get the total number of Raman NBT molecules per single nanorod $N_1 = 1.8 \times 10^4$. Finally, the total number of SERS molecules per one L is $N_{NBT} = 3.9 \times 10^{13}(\mathrm{L}^{-1}) \times 1.8 \times 10^4 = 7.02 \times 10^{18}(\mathrm{L}^{-1}) = 1.17 \times 10^{-6}\,\mathrm{M}$. Compared to other estimations of the surface molecular covering,[4] the above number is an upper limit, and our estimate of the average SERS EF should therefore be considered a lower limit.

The measured surface normalized SERS intensity at 1342 cm^{-1} equals 964 counts for NBT concentration $c_{NBT} = 1.17 \times 10^{-6}\,\mathrm{M}$, whereas the normal Raman intensity equals 10000 counts for concentration $c_{NBT} = 0.15\mathrm{M}$. After substitution of all quantities into relation (S15) we finally get

$$EF = \frac{964 / 1.17 \times 10^{-6}}{1 \times 10^{4} / 0.15} = 1.23 \times 10^{4}. \qquad \text{(S15)}$$

Although the estimate (S15) can be inaccurate, for our purposes it is important the range of possible variations in the number of Raman active molecules in etched samples. It is instructive to compare this assumption with the direct experimental measurements of the surface covering of AuNRs by methylene blue reported by Sivapalan et al.[4] By using the electrospray ionization liquid chromatography mass spectrometry, they found a roughly constant number of adsorbed molecules per one nanorod 125 ± 25 for AuNR aspect ratios ranging from 2.5 to 4.5. For shorter AuNRs, the number of adsorbed molecules was of about 200. In our experiments, the ratio of the total surface areas (or, in other words, the total numbers of Raman adsorbed molecules) for the initial and final AuNRs roughly equals 2:1. Thus, our assumption about small variations in the number of Raman active molecules per one etched nanorod is in qualitative agreement with the experimental data reported by Sivapalan *et al*.[4]

Section S8. Quantifying the gold concentration in etched samples by AAS

For quantifying the number of gold nanorods and number of adsorbed NBT molecules, we prepared three AuNR-700, AuNR-788, and AuNR-890 samples by etching the initial AuNR-916 sample (Figure S6).

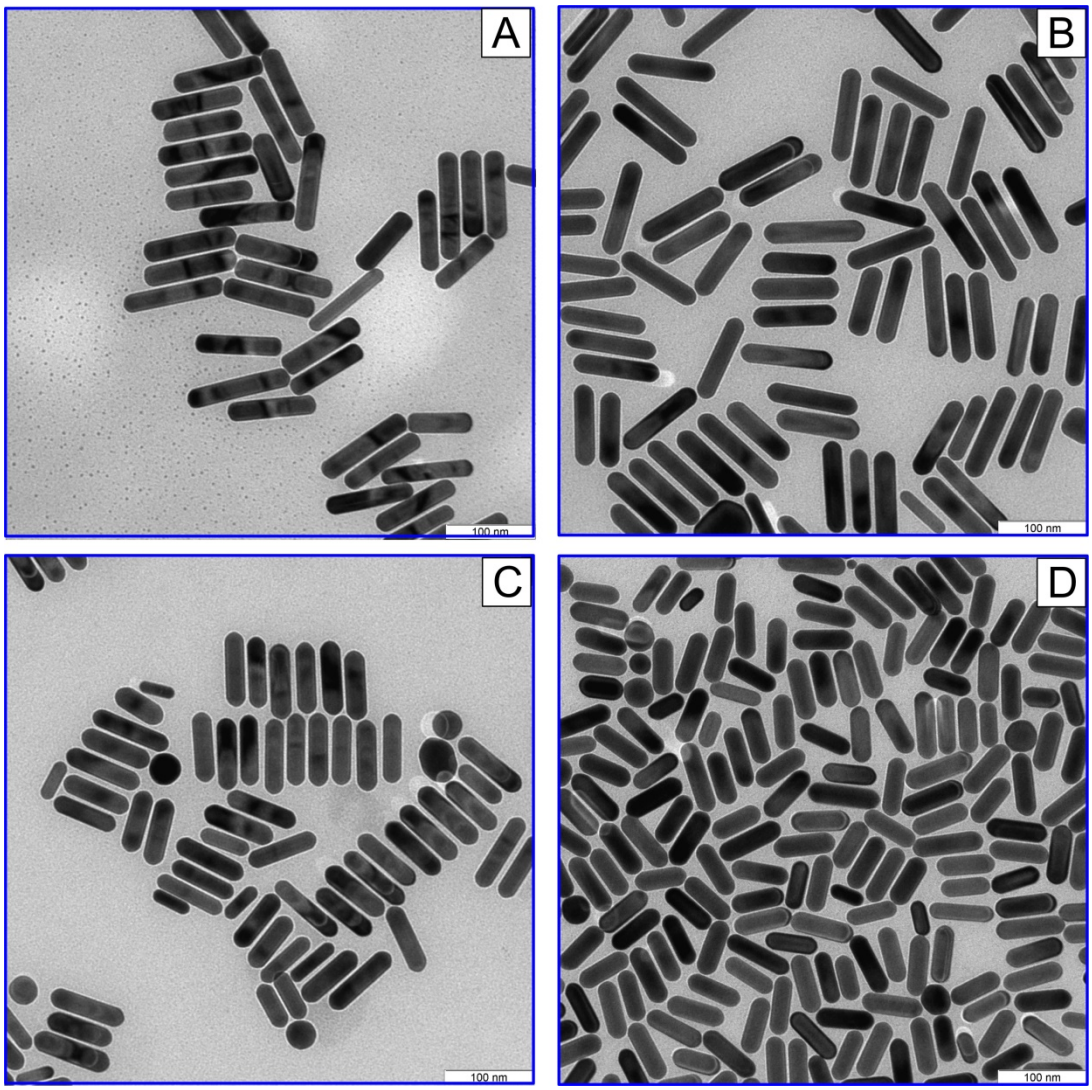

Figure S6. TEM images of AuNR-916 (A), AuNR-890 (B), AuNR-788 (C), and AuNR-700 (D) samples. The scale bars are 100 nm.

The statistical geometrical parameters of AuNRs are summarized in Table S3.

Table S3. PR wavelength, length, width and aspect ratio of the initial and etched AuNRs (Set 3)

Sample	PR wavelength, nm	Length, nm	Width, nm	Aspect ratio, AR
AuNR-916	916	105.2±7.4	22.6±1.2	4.68±0.43
AuNR-890	890	100.8±7.8	23.1±1.8	4.30±0.39
AuNR-788	788	81.8±7.9	23.0±1.3	3.55±0.25
AuNR-700	700	66.3±4.0	22.9±1.5	2.86±0.23

Table S4. Gold concentrations C_{Au} (mg/L) determined by AAS (methods 1 and 2). The nanorod concentrations are calculated as $N = C_{Au} / m_1$ (part/mL), where the average nanorod mass m_1 was obtained from TEM data.

Sample	Mass m_1, fg	AAS, method 1		AAS, method 2	
		C_{Au} mg/L	N $\times 10^{10}$ part/mL	C_{Au} mg/L	N $\times 10^{10}$ part/mL
AuNR-890	0.749	56.7±0.01	7.57	53.7±0.24	7.17
AuNR-788	0.599	45.9±0.12	7.66	37.1±0.43	6.19
AuNR-700	0.456	33.2±0.31	7.28	27.4±0.78	6.01

Table S4 shows a reasonable agreement between two sets of gold concentrations determined by AAS through methods 1 and 2 (see Methods section in the main text). What is more, the nanorods concentrations in three etched samples are roughly constant, in agreement with our assumption based on chemistry of nanorod etching.

Section S9. Quantifying the gold concentration in etched samples by UV-vis spectrophotometry

For determination of gold concentration in etched samples we rewrite Eq. (S9) as

$$c_g = \frac{A_{\max}^{\exp} \ln 10 \rho_g V_t}{l \langle C_{ext} \rangle}, \tag{S16}$$

where $A_{\max}^{\exp}$ is the experimental extinction peak value and all other parameters are defined in Section S2. The statistical parameters of AuNR ensembles were derived from TEM images (Table S3) and were used for calculation of theoretical spectra by the T-matrix method as described in Section S2. Finally, Eq. (S16) was used to calculate the fitting gold concentration at which the experimental and theoretical peak values coincide (Figures S7, S8).

Figure S7A shows the experimental extinction spectra of the initial nanorods AuNR-916 and three etched samples. Figures S7B and S8 give a comparison of the experimental and calculated extinction spectra for the initial AuNR-916 sample and for three etched samples, respectively. These examples illustrate the use of Eq. (S16) for determination of the mass-volume gold concentration in AuNR colloids.

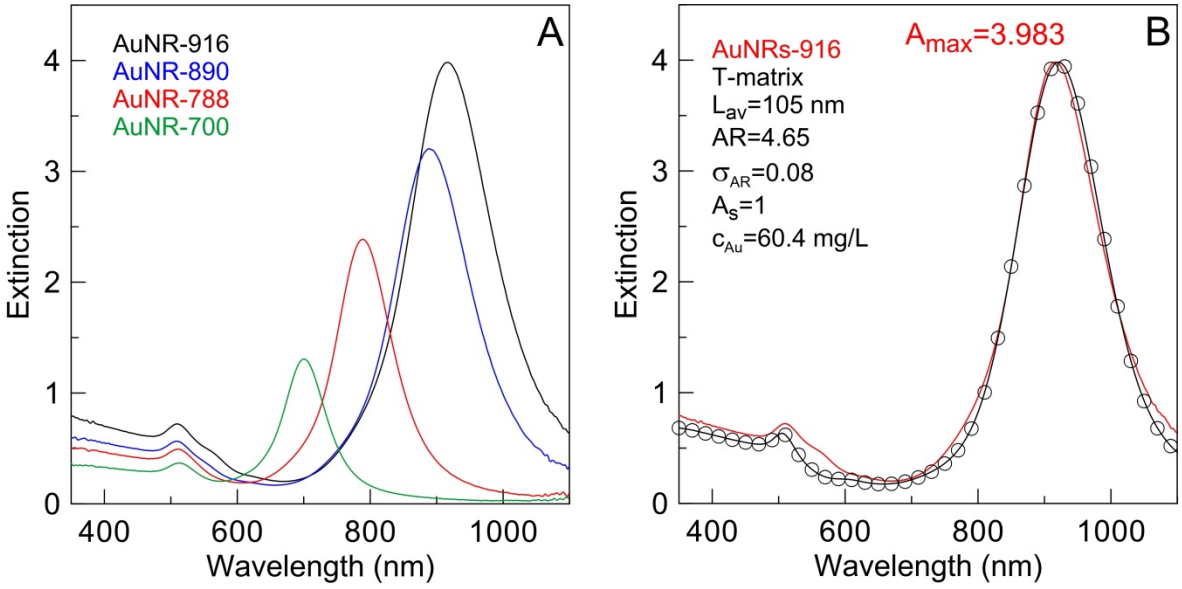

Figure S7. (A) Extinction spectra of the initial (AuNR-916) and three etched samples AuNR-890, AuNR-788, and AuNR-700. (B) Experimental (red curve) extinction spectrum of AuNR-916 sample. Black circles show the T-matrix simulated spectrum calculated with TEM-derived parameters indicated on the plot: the average length $L_{av} = 105$ nm, the average aspect ratio is

$AR = 4.65 \times (1 \pm 0.08)$. The gold concentration $c_{\mathrm{Au}} = 60.4$ mg/L was used as a fitting parameter for theoretical plasmonic peak value. The electron scattering constant is $A_s = 1$.

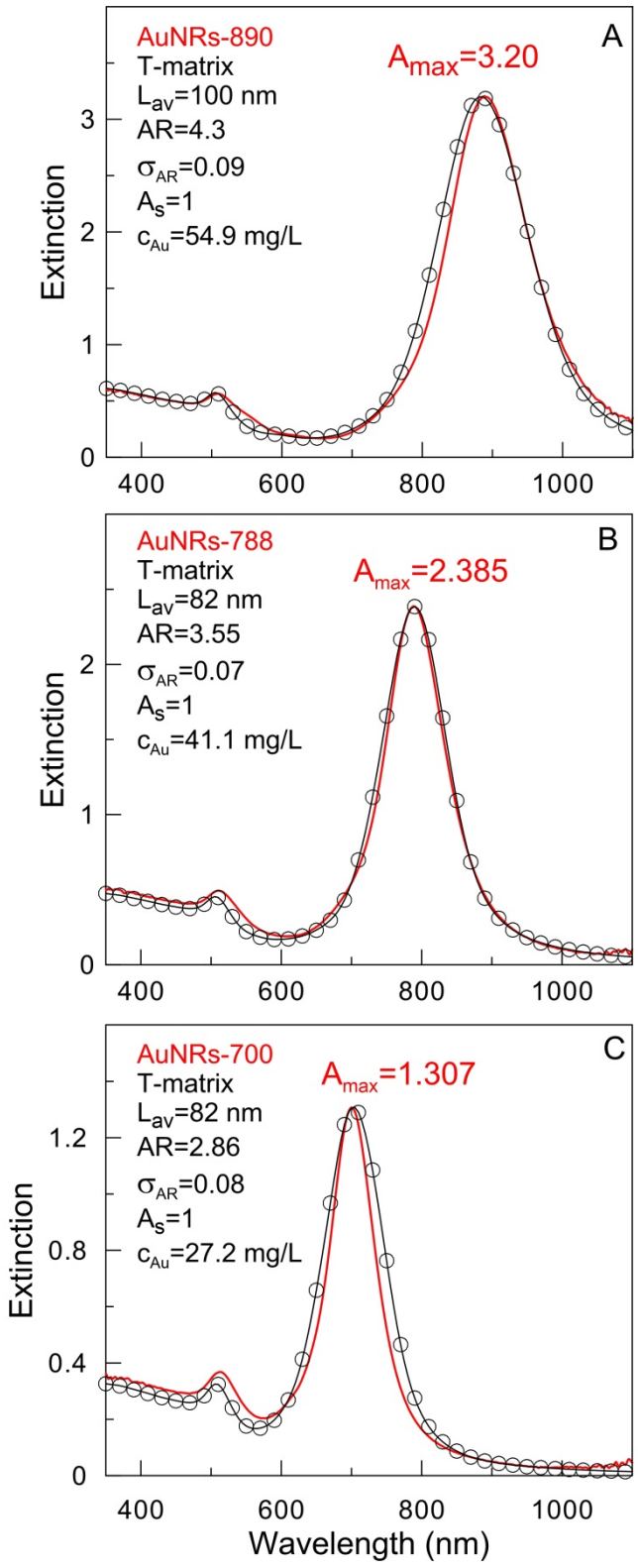

Figure S8. Experimental (red curves) and T-matrix simulated (circles) spectra of AuNR-890 (A), AuNR-788 (B), and AuNR-700 (C) samples with TEM-derived parameters indicated on the plots. The gold concentrations were found from Eq. (S16).

In Eq. (S16), the average extinction cross section is very sensitive to the model parameters such as the particle size and shape distribution and the optical constants of particles.[5] As a result, Eq. (S16) can predict concentrations within a broad range. That is why we used another approach based on measurements of absorption for 400-450 nm wavelengths.[6] In this spectral band, the absorption of gold colloids is determined by the absorption of *d*-electrons in gold particles thus making the colloidal absorption not too sensitive to the particle shape and structure. In fact, the key absorption parameter is the particle volume. Therefore, the experimental measurements of absorption can be used for determination of the gold concentration in the same way as for plasmonic peak measurements, with a modified form of Eq. (S16) in which $A_{\max}^{\exp}$ is replaced with $A_{450}^{\exp}$ or $A_{400}^{\exp}$.

Haiss et al.[6] tabulated the molar decadic extinction coefficient $\varepsilon_{450}(\mathrm{M^{-1}cm^{-1}})$ determined by the known Bouguer law

$$J = J_0 10^{-A_{450}} = J_0 10^{-\varepsilon_{450}(\mathrm{M^{-1}cm^{-1}})\cdot c(\mathrm{M})\cdot l(\mathrm{cm})}. \tag{S17}$$

$$\varepsilon(\mathrm{M^{-1}cm^{-1}}) = \frac{A_{ext}}{c_{\mathrm{AuNP}}(\mathrm{M})\, l(\mathrm{cm})}. \tag{S18}$$

Note that $c(\mathrm{M})$ is the molar concentration of particles

$$c_{\mathrm{AuNP}}(\mathrm{M}) = N(\mathrm{part/mL}) / 6\times 10^{20}, \tag{S19}$$

rather than the gold concentration $c(\mathrm{mg/L})$. For a given mass-volume concentration of an AuNR suspension $c(\mathrm{mg/L})$, the molar extinction coefficient can be calculated by relation

$$\varepsilon(\mathrm{M^{-1}cm^{-1}}) = 495\times 10^5 \frac{A_{450} a_{0ev}^3}{c(\mathrm{mg/L})}. \tag{S20}$$

Because the tabulated data of Ref.[6] were obtained by Mie theory, they are not applicable to AuNR suspensions. We have performed T-matrix calculations of the molar extinction coefficient by using (Eq. S18) for AuNRs with length from 10 to 150 nm and diameters from 10 to 30 nm (Figure S9). The gold concentration $c = 57\text{mg/L}$ is constant and corresponds to 0.01% solution of $HAuCl_4$. For other concentrations, the molar extinction coefficients can be easily recalculated by Eq. (S20).

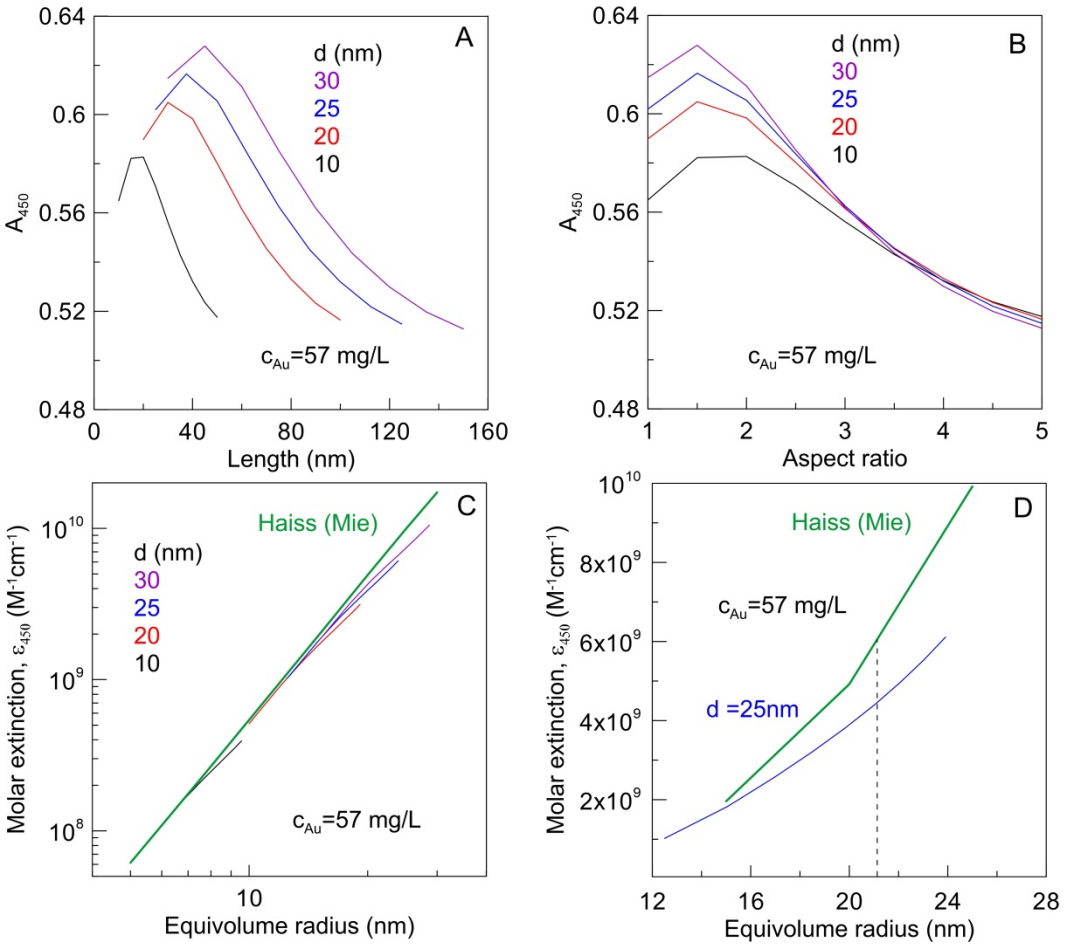

Figure S9. Dependence of the extinction A_{450} on the nanorod length (A) and aspect ratio (B) at different diameters from 10 to 30 nm. Note that for aspect ratios higher than 2.5 all curves collapse into one universal dependence. (C) Dependence of the molar extinction coefficient on the equivolume sphere radius at four constant nanorod diameters from 10 to 30 nm. The green line shows the Mie data by Haiss *et al.* [6] The panel D explains why the Mie theory gives underestimated gold concentrations (roughly by 50%) for our nanorods with equivolume radius 21 nm.

Table S5 summarizes data on calculated cross sections and determined concentrations of gold and nanorods for three etched samples.

Table S5. Extinction cross section of AuNRs calculated by the T-matrix method, gold concentration $C_{\mathrm{Au}}(\mathrm{mg/L})$ and the nanorod concentration $N(\mathrm{part/mL})$ determined from the experimental extinction at PR wavelength and at 450 nm

Sample	$\langle C_{ext}^{PR} \rangle$ $(\times 10^4\,\mathrm{nm}^2)$	$\langle C_{ext}^{450} \rangle$ $(\times 10^4\,\mathrm{nm}^2)$	C_{Au}(mg/L) by A_{PR}	C_{Au}(mg/L) by A_{450}	N_{PR} $\times 10^{10}\,\mathrm{mL}^{-1}$	N_{450} $\times 10^{10}\,\mathrm{mL}^{-1}$
AuNR-890	1.01	0.157	54.9	54.6	7.31	7.27
AuNR-788	0.799	0.129	41.1	44.5	6.87	7.44
AuNR-700	0.511	0.104	27.2	30.3	5.92	6.57

Section S10. Quantifying the number of NBT molecules adsorbed on gold nanorods

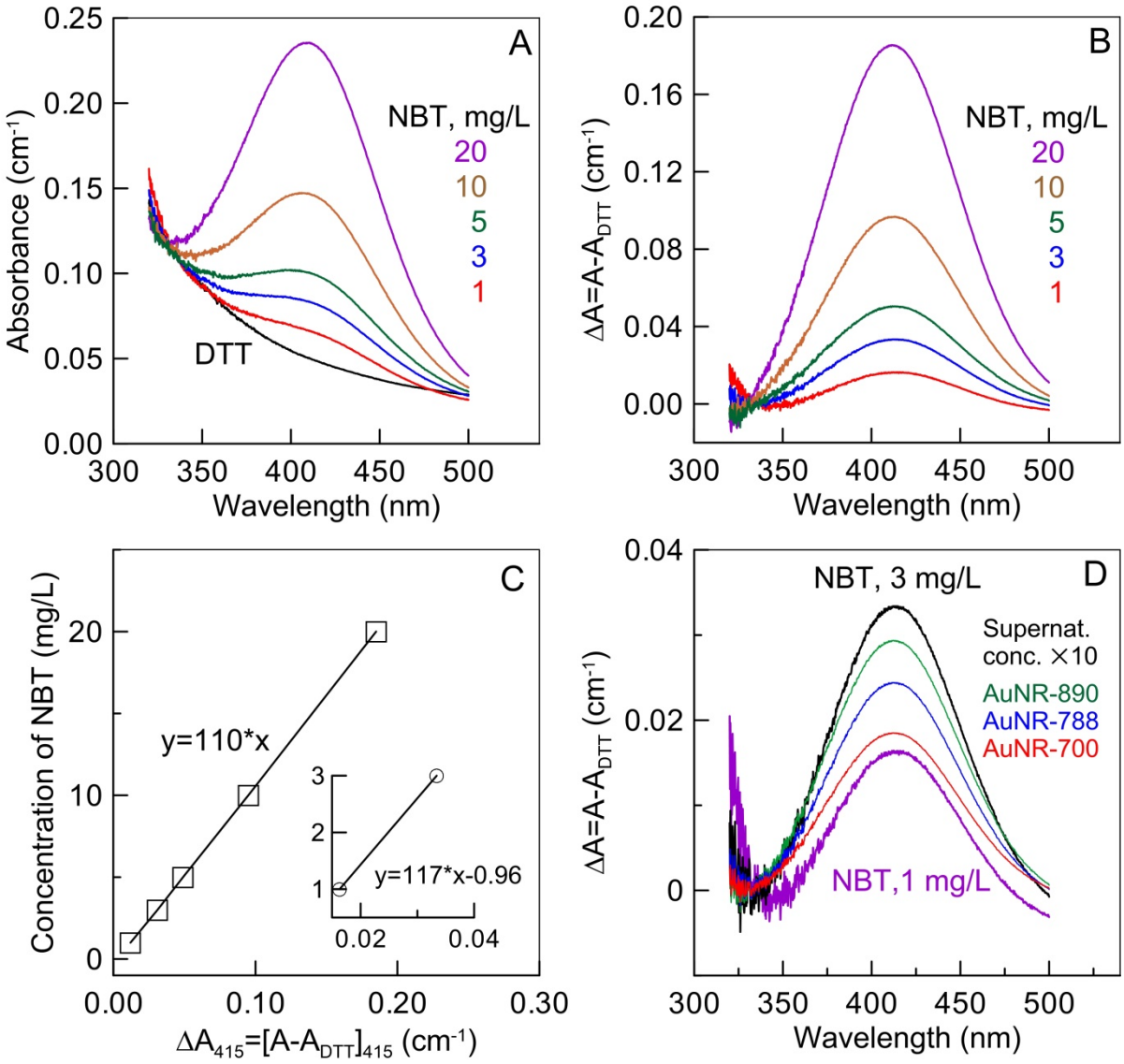

Figure S10. (A) Absorption spectra of DTT blank solution (black) and solutions of NBT with concentrations from 1 to 20 mg/L. (B) Differential absorption spectra of NBT solutions after subtraction of DTT absorbance. (C) The calibration dependence of the NBT concentration as a function of the differential absorbance at 415 nm. The inset shows enlarged portion at small concentrations. (D) Differential absorption spectra of calibration solutions with 3 mg/L and 1 mg/L NBT and supernatants with desorbed NBT molecules for three concentrated (×10) AuNR@NBT samples. The desorbed NBT concentrations are 0.25, 0.195, and 0.123 mg/L for non-concentrated AuNR-890@NBT, AuNR-788@NBT and AuNR-700@NBT samples, respectively.

Figure S10 illustrates quantifying the NBT concentration of molecules adsorbed on AuNRs. The panel D plots shows that the concentrations of desorbed NBT molecules for three concentrated ($\times 10$) AuNR samples are between 1 and 3 mg/L. Now we have all data for quantifying the number of NBT molecules per one nanorod. The number of adsorbed NBT molecules equals $N_{NBT} = c_{NBT} \times N_A / M_{NBT}$, where the molar mass of NBT equals 155 g/mol and the Avogadro number is $N_A = 6 \times 10^{23}$ mol^{-1}. The number of adsorbed NBT molecules per one nanorod is $N^1_{NBT} = N_{NBT} / N_{AuNR}$. The ratio of the surface area of one nanorod $S_1(\text{nm}^2)$ to the number of adsorbed molecules N^1_{NBT} gives the experimental estimate of the NBT adsorption footprint $S^1_{NBT} = S^1_{AuNR} / N^1_{NBT}$, which can be compared with the topological polar surface area of NBT 0.468 nm^2 (Ref.[3]).

Table S6. Quantifying the adsorption of NBT molecules on gold nanorods

Sample	c_{NBT} mg/L	N $\times 10^{10}$ part./mL	N^1_{NBT} $\times 10^4$	S^1_{AuNR} $\times 10^3$ nm^2	$S^1_{NBT} = S^1_{AuNR} / N^1_{NBT}$ nm^2
AuNR-890@NBT	0.25	7.33±0.17	1.33	7.32	0.55
AuNR-788@NBT	0.195	7.04±0.66	1.08	5.91	0.55
AuNR-700@NBT	0.123	6.45±0.63	0.757	4.77	0.64

Section S11. SERS spectra and enhancement factors for Set 3 of AuNRs.

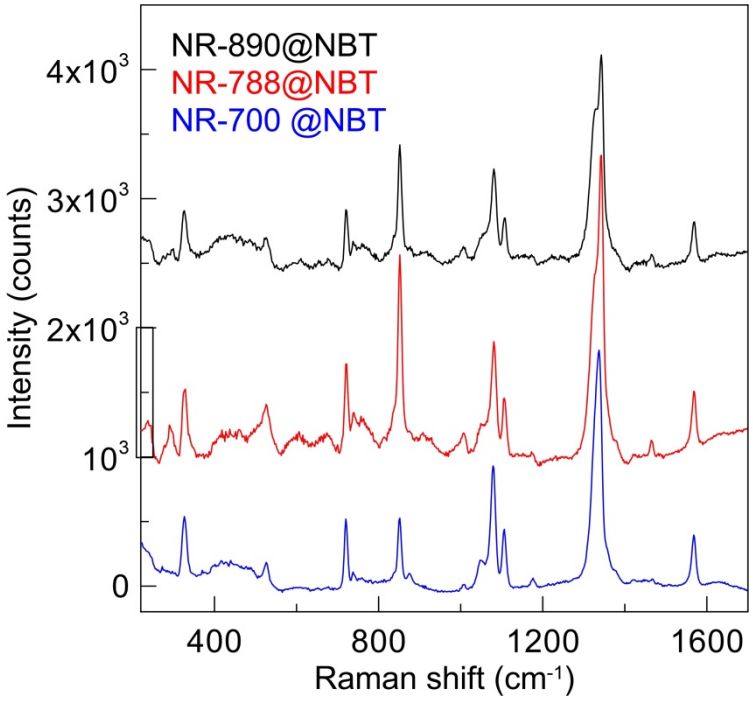

Figure S11. SERS spectra of NBT molecules adsorbed on three etched AuNR samples.

Table S7. SERS enhancement factors for Set 3 of etched AuNRs.

Sample	c_{NBT} μM	I_{1340} $\times 10^3$ counts	I_{Raman} 0.15M NBT $\times 10^4$ counts	$EF = \frac{I_{1340} / c_{NBT}(\text{M})}{I_{Raman} / 0.15\text{M}}$
AuNR-890@NBT	1.61	1.63	1	1.5×10^4
AuNR-788@NBT	1.26	2.35	1	2.8×10^4
AuNR-700@NBT	0.81	1.76	1	3.25×10^4

References.

(1) Khlebtsov N.G. Orientational Averaging of Light-Scattering Observables in the T-matrix Approach. *Appl. Opt*. **1992**, *31*, 5359–5365.

(2) Khlebtsov, B.; Khanadeev, V.; Pylaev, T.; Khlebtsov N. A New T-Matrix Solvable Model for Nanorods: TEM-Based Ensemble Simulations Supported by Experiments. *J. Phys. Chem. C* **2011**, *115*, 6317–6323.

(3) URL: https://pubchem.ncbi.nlm.nih.gov/compound/4-Nitrothiophenol

(4) Sivapalan, S.T.; DeVetter, B.M.; Yang, T.K.; van Dijk, T.; Schulmerich, M.V.; Carney, P.S.; Bhargava, R.; Murphy, C.J. Off-Resonance Surface-Enhanced Raman Spectroscopy from Gold Nanorod Suspensions As a Function of Aspect Ratio: Not What We Thought. *ACS Nano* **2013**, *7*, 2099–2105.

(5) Khlebtsov, N. G. Determination of Size and Concentration of Gold Nanoparticles from Extinction Spectra. *Anal. Chem.* **2008,** *80,* 6620–6625.

(6) Haiss, W.; Thanh, N. T. K.; Aveard, J.; Fernig, D. G. Determination of Size and Concentration of Gold Nanoparticles from UV-Vis Spectra. *Anal. C*hem. **2007**, *79*, 4215–4221.